A&A, 691, A193 (2024)
https://doi.org/10.1051/0004-6361/202451580

Astronomy & Astrophysics

The twisted jets and magnetic fields of the extended radio galaxy 4C 70.19⋆

M. Weżgowiec[1,⋆⋆], M. Jamrozy[1], K. T. Chyży[1], M. J. Hardcastle[2], A. Kuźmicz[1], G. Heald[3], and T. W. Shimwell[4]

[1] Obserwatorium Astronomiczne Uniwersytetu Jagiellońskiego, ul. Orla 171, 30-244 Kraków, Poland
[2] Centre for Astrophysics Research, Department of Physics, Astronomy and Mathematics, University of Hertfordshire, College Lane, Hatfield AL10 9AB, UK
[3] CSIRO Astronomy and Space Science, PO Box 1130, Bentley, WA 6102, Australia
[4] ASTRON, the Netherlands Institute for Radio Astronomy, Postbus 2, 7990 AA Dwingeloo, The Netherlands

Received 19 July 2024 / Accepted 16 September 2024

ABSTRACT

Context. The appearance of the jets and lobes of some radio galaxies makes it difficult to assign them to a known class of objects. This is often due to the activity of the central engine and/or interactions with the environment, as well as projection effects.
Aims. We analyse the radio data for an apparently asymmetric radio source 4C 70.19, which is associated with the giant elliptical galaxy NGC 6048. The source shows distorted radio jets and lobes, one of which bends by 180°. The aim of our study is to explain the nature of the observed distortions.
Methods. We used LOFAR, Effelsberg, and VLA radio data in a wide range of frequencies. At high frequencies, we also used radio polarimetry to study the properties of the magnetic fields. Additionally, we made use of optical, infra-red, and X-ray data.
Results. Polarisation data suggest shearing of the magnetic fields at points where the jets bend. The low-frequency LOFAR map at 145 MHz, as well as the sensitive single-dish Effelsberg map at 8.35 GHz, reveal previously undetected diffuse emission around the source. The rotation measure (RM) derived from the polarimetric data allowed us to estimate the density of the medium surrounding the source, which agrees with typical densities of the intergalactic medium or the outer parts of insterstellar halos.
Conclusions. We propose that the southern jet is bent in the same manner as the northern one, but that it is inclined to the sky plane. Both these bends are likely caused by the orbital motion within the galaxy group, as well as interactions with the intergalactic medium. Our analyses suggest that, despite its complex morphology, 4C 70.19 seems to be intrinsically symmetric with a physical extent of up to 600 kpc, and that the diffuse emission detected in our high-sensitivity maps is related to radio plumes that are expanding behind the source.

Key words. galaxies: active – galaxies: individual: NGC 608 – galaxies: individual: 4C70.19 – galaxies: jets – galaxies: magnetic fields – radio continuum: galaxies

1. Introduction

Radio galaxies (RGs) are known to possess an active galactic nucleus (AGN), which is responsible for the production of jets and lobes, often extending far from the host galaxy to distances of tens to hundreds of kiloparsecs (kpc) or even up to several megaparsecs (Mpc), as reported by, for example, Machalski et al. (2008), Kuźmicz et al. (2018), or Dabhade et al. (2020). It is clear that those jets and lobes must interact with the surrounding intergalactic medium (IGM). In the case of objects that form part of a larger system (galaxy groups or clusters), the interactions also include the gravitational influence experienced by the source along its orbit (e.g. Vallée et al. 1981; Horellou et al. 2018). Simultaneously, the same kinds of interactions can stimulate AGN activity. The complex morphology of the radio jets and lobes of RGs often suggests an episodic activity of the central source or the influence of the orbital motion within their group or cluster environment. Recurrent activity has been reported in a number of sources (e.g. Saikia & Jamrozy 2009; Nandi & Saikia 2012; Kuźmicz et al. 2017; Mahatma et al. 2019, and references therein).

In this paper, we present the results of our investigation of the radio galaxy 4C 70.19, the radio jets of which appear to have a distorted morphology, including an unusual, asymmetric structure with a 'hook-like' jet on one side (Lara et al. 2001). The source does not show prominent hot spots and was recognised by Lara et al. (2001) as an FRI source (Fanaroff & Riley 1974). However, the brightenings of the outer parts of the source, which form lobe-like structures, require further investigation. To analyse and explain the morphology of 4C 70.19, we gathered data over a wide range of radio frequencies, from LOw-Frequency ARray (LOFAR; van Haarlem et al. 2013) data at 145 MHz to sensitive single-dish Effelsberg observations at 8.35 GHz. The high-frequency radio data enable polarisation studies, which allowed us to examine the properties of the magnetic fields throughout the entire radio source. Sensitive single-dish observations above 1.4 GHz allowed us to study the evolution of relativistic electrons in 4C 70.19, which led to reliable determinations of the spectral index profiles and both the dynamical and synchrotron age. To further study the intergalactic environment

⋆ Based on observations with the 100-m telescope at Effelsberg operated by the Max-Planck-Institut für Radioastronomie (MPIfR) on behalf of the Max-Planck-Gesellschaft.
⋆⋆ Corresponding author; markmet@oa.uj.edu.pl

of 4C 70.19, we also analysed the vicinity of this source using archival X-ray, optical, and infrared data.

Throughout this paper we use a cosmological model in which $H_0 = 71\,km\,s^{-1}\,Mpc^{-1}$, $\Omega_M = 0.27$, and $\Omega_\Lambda = 0.73$ (Spergel et al. 2003). This translates the redshift of the source, of $z = 0.0257$, to a co-moving distance of 108 Mpc (1 arcminute corresponds to 30 kpc).

4C 70.19 is associated with the bright (R ≃ 12.7 mag) galaxy NGC 6048 (also known as UGC 10124), located at Right Ascension (RA) = $15^h57^m30\overset{s}{.}2$, (Dec.) = $+70°41'21\overset{''}{.}0$ (J2000.0). In the optical spectrum of NGC 6048, only absorption lines are present (Stickel et al. 1993), which suggests that the central AGN is accreting at a low level, which in turn is typical for an FRI source (Hine & Longair 1979). Schombert (2015) classified NGC 6048 as a D-class elliptical galaxy, being the result of a recent equal-mass dry merger, that is, of two gas-poor galaxies (no energy dissipation via the gaseous component).

The radio structure of 4C 70.19 has a large angular extent of about 11′ in the N–S direction, which corresponds to a projected linear size of about 330 kpc. The large angular size enables studies of the physical conditions throughout the source. The extended radio morphology of 4C 70.19, with a bright core, jets, and radio plumes, resembles that of an FRI-type RG, and the source has a total 1400 MHz radio power of log(P) = $24.5\,W\,Hz^{-1}$, which is below the canonical FRI/FRII luminosity break. A closer look, however, reveals some unusual features. Previous radio observations with NVSS show that the northern radio jet is bent by around 180° and then extends into a plume-like structure. On the contrary, the southern jet, which has a relatively typical morphology, is slightly deviated from the main axis of the radio source. No prominent compact hot spots have been detected in the high-frequency high-resolution maps (e.g. Lara et al. 2001).

Throughout the paper we use two names for our studied source: we use 4C 70.19 whenever radio data are analysed, and NGC 6048 when discussing other data referring to the host galaxy.

2. Observations and data reduction

In this paper, we use LOFAR survey data and Effelsberg observations, as well as other archival radio data. To reveal the nature of 4C 70.19, our study also uses infrared maps from the Wide-field Infrared Survey Explorer (WISE; Wright et al. 2010) and X-ray data from the ROentgen SATellite (ROSAT; Truemper 1982) High-Resolution Imager (HRI; Pfeffermann et al. 1987).

2.1. Radio data

2.1.1. LOFAR

The inspection of an early LOFAR Multifrequency Snapshot Sky Survey image (MSSS; Heald et al. 2015) revealed that the morphology of 4C 70.19 is significantly different at low frequencies, showing a typical straight northern radio lobe. Its bend, however, known from the radio maps at higher frequencies, was confirmed by the deeper LOFAR Two-metre Sky Survey (LoTSS; Shimwell et al. 2017) images. The LoTSS data were first processed using a direction independent calibration pipeline (see e.g. van Weeren et al. 2016; Williams et al. 2016; de Gasperin et al. 2019). After this the data were processed by the latest version of DDF-pipeline[1], which makes use of kMS (Tasse 2014; Smirnov & Tasse 2015) for calibration and DDFacet (Tasse et al. 2018) for imaging. This pipeline is described in detail in Shimwell et al. (2019) and Tasse et al. (2021). We used the data from the LoTSS pointing P232+70 (proposal code LC10_013). Our target galaxy is 2.°3 from the pointing centre (59% of the peak primary beam response). In this paper, we present the radio map of 4C 70.19 in the 120–168 MHz band with a central frequency of 145 MHz (Fig. 1). The sensitivity r.m.s level in the vicinity of the source is 0.2 mJy beam^{-1} (see Table 1 for details).

2.1.2. Effelsberg

We performed high-frequency radio polarimetry of 4C 70.19. The observations at 4.85 and 8.35 GHz were performed in May 2014 (project number 117-13) and at 2.67 GHz in November 2014, using the 100-m Effelsberg radio telescope of the Max-Planck-Institut für Radioastronomie[2] (MPIfR) in Bonn. At 4.85 GHz the observations were performed using the two-horn system (with a horn separation of 8′) at the secondary focus (see Gioia et al. 1982). Each horn was equipped with two total power receivers and an IF polarimeter resulting in four channels containing the Stokes parameters I (two channels), Q and U. The telescope pointing was corrected by performing cross-scans of a bright point source close to the observed RG. The flux density scale was established by mapping the point source 3C 286 and aligning its flux with the scale of Baars et al. (1977). The same source was also used for polarisation calibration. To map the source at 4.85 GHz with the dual-beam receiver, scans in the azimuth-elevation frame were obtained. At 2.67 and 8.35 GHz (single horn receivers), maps were obtained by alternately scanning along the RA and Dec. directions. The data reduction was performed using the NOD2 data reduction package (see Weżgowiec et al. 2007, for details). In the case of data at 2.67 GHz we could not use the broadband channel, as some of the frequencies were heavily affected by the RFI. Instead, two distorted channels were excluded and the remaining data from six channels were used.

2.1.3. Archival radio data

This paper also uses archival VLA data at 1.43 and 4.85 GHz, which were reduced using the AIPS package[3]. The WENSS map at 327 MHz was also used in its original version to provide data for spectral analysis of the source.

At 1.43 GHz we used VLA C-configuration data from project AL442. For the flux density scale we used the radio source 3C 138, which also served for the calibration of the polarisation angle. The phase calibration was performed with the use of the radio sources J1435+760 and J1748+700.

At 4.85 GHz two data sets in C (project BT012B) and D (project AW269) configurations of the VLA were used. For both data sets the flux density scale and polarisation angle calibration was performed with the use of the radio source 3C 286. The phase calibration was done using the radio sources J1531+721 and J1642+689 for C and D configurations, respectively. To ensure both high resolution and sensitivity to large-scale radio emission, the calibrated data from both configurations were combined prior to imaging with the AIPS task DBCON.

The image deconvolution from the calibrated VLA data was performed using the Clark CLEAN algorithm (Clark 1980) and

[1] https://github.com/mhardcastle/ddf-pipeline

[2] http://www.mpifr-bonn.mpg.de

[3] http://aips.nrao.edu

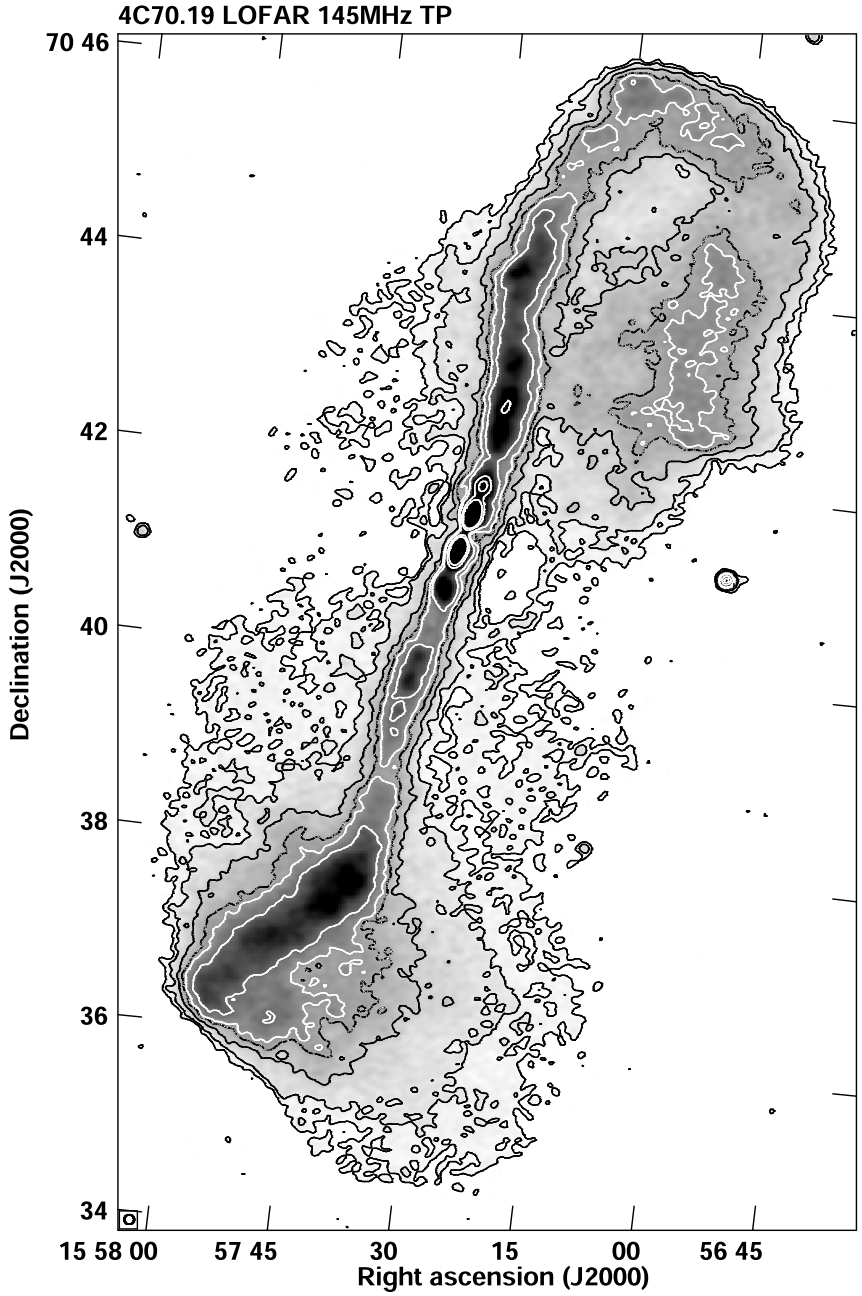

Fig. 1. LOFAR map of 4C 70.19 at 145 MHz with contours of (3, 6, 12, 18, 22, 30, 64, and 96) × 0.2 mJy beam^{-1}. The beam size of 6″ is shown in the bottom left corner of the image. The compact object below the northern plume is an unrelated background source.

Table 1. Radio maps and fluxes of 4C 70.19.

Freq. [MHz]	Telescope	Beam size [″]	r.m.s. [mJy beam^{-1}]	Total flux [Jy]
145	LOFAR	6	0.20	9.29±0.47
327	WSRT	60	7.00	5.15±0.26
1430	VLA	34	0.37	2.60±0.13
2674	Effelsberg	264	3.50	1.55±0.08
4850	VLA+Effelsberg	15	0.29	1.03±0.05
8350	Effelsberg	82	0.31	0.76±0.04

resulted in elliptical beams of the clean maps. Each beam was later convolved to a circular one. Because of the large angular extent of 4C 70.19, the observations at 4.85 GHz, due to the largest angular scale of only around 4′ at both C and D configurations[4], suffer from a lack of information about the large-scale emission. Therefore, we show these data only in combination with the corresponding single-dish Effelsberg maps.

The combination of maps was performed in the spatial frequency domain image plane using the AIPS task IMERG. The task Fourier-transforms the images to the (u,v) plane, normalises amplitudes within the annulus of overlap in the (u,v) plane and back transforms the combined data to the image plane. The normalisation uses the ratio of the resolutions of the input images. To verify the quality of the combined maps, we compared the flux densities in the Effelsberg maps with those in the combined maps and found that the fluxes agree within 3%.

[4] https://science.nrao.edu/facilities/vla/docs/manuals/oss/performance/resolution

2.1.4. Polarisation radio data

From the Effelsberg and the VLA radio data we obtained maps of the polarised emission, as well as the polarisation angle maps. These maps were then used to plot the so-called B-vectors, which show the orientation of the magnetic field (polarisation angle of the E-vectors rotated by 90°). The length of the B-vectors is presented as proportional to the polarised intensity. The maps of the polarisation angle were also used to produce maps of the RM, which provide information about the magnetic field along the line of sight and help to estimate the density of the IGM around 4C 70.19 (see Sect. 4.2.1 for details).

2.2. Other data

The available pipeline products of the ROSAT HRI pointed observations (Dataset ID rh701836N00) of NGC 6048 were used to obtain the HRI map of the X-ray emission and the countrate of the core region. The latter allowed us to estimate the luminosity of the central source of 4C 70.19. The HRI map was adaptively smoothed in the full energy range of the instrument using the ASMOOTH task from the XMM-Newton Science Analysis System (SAS; Gabriel et al. 2004) package.

From the WISE archives maps in all 4 energy bands covered by the telescope (W1 – 3.4 μm, W2 – 4.6 μm, W3 – 12 μm, and W4 – 22 μm) were acquired to trace the dust emission in the main body of NGC 6048.

We also made use of several optical catalogues, as well as the Pan-STARRS data (Flewelling et al. 2020), to obtain information about the group environment of NGC 6048, including its closest companions (see Sect. 4.1).

3. Results

3.1. Radio maps

Sensitive radio maps of 4C 70.19 in a wide range of frequencies and resolutions (see Table 1) allowed us to study the morphology of both radio jets (also within the host galaxy) and of the radio envelope.

The capabilities of the LOFAR telescope allowed us to detect both the diffuse extended emission around the source and fine details of the radio jets, also within the host galaxy (Figs. 1 and 2). Unlike in the high frequency maps of Lara et al. (2001), in the 145 MHz LOFAR map the central source of 4C 70.19 is not visible. The two distinct inner structures that are likely bases of the jets, also detected by Lara et al. (2001), are well resolved. The jets extending further out are not coaxial and change their direction. The high resolution of the map confirms that at low frequencies the morphology of the source is very similar to that found in the high frequency maps and that the northern plume is formed by a jet, which changes its direction by 180°. The southern jet also bends significantly towards southeast and the visible kink at its end suggests that also in the south a significant change in the direction of the jet is observed. In particular, more diffuse emission extends to the west, which may mark the southern plume, oriented not directly in the sky plane. Around the bright jets some diffuse large-scale emission can be traced. Its patchy appearance likely originates from the low sensitivity to faint large-scale structures of the small beam of the observations. The large-scale diffuse radio emission at low frequencies will be discussed in Sect. 4.2.

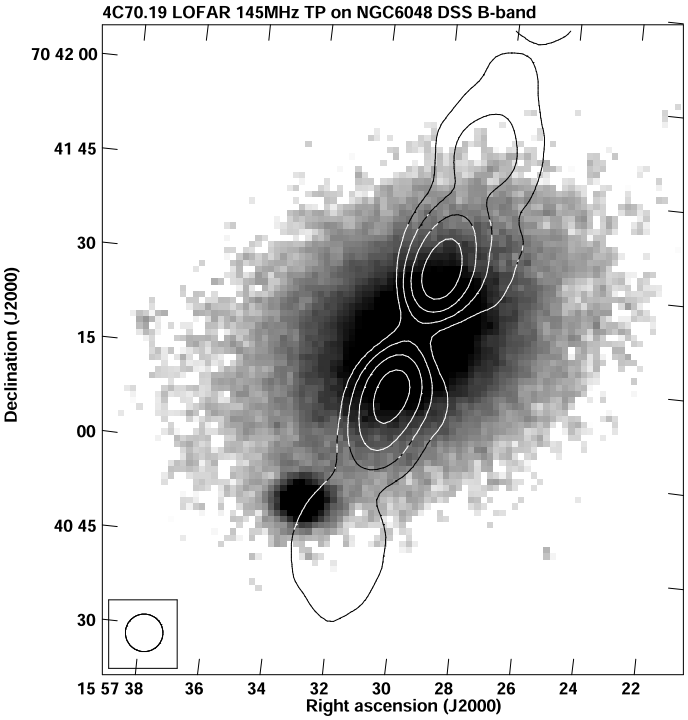

Fig. 2. LOFAR map of radio total power at 145 MHz of the inner jet structures overlaid on the DSS B-band image. The contours are (32, 64, 128, and 256) × 0.2 mJy beam^{-1}. The resolution of the map is 6″.

The zoomed-in central part of the LOFAR map overlaid on the DSS[5] optical image of NGC 6048 (Fig. 2) shows that the bases of the jets reside within the main body of the galaxy, slightly extending into the halo, where the secondary brightenings are present.

The WSRT map at 1′ resolution at 327 MHz from the WENSS survey (Fig. 3) shows the global morphology of the source. The hook-like shape of the northern jet is only slightly resolved. On both sides of the source the emission surrounding the jet regions does not extend farther than that visible in the LOFAR map.

The core region of 4C 70.19 and the bend of the northern jet becomes resolved in the VLA map at 1.43 GHz (Fig. 4). Also the elongated area of higher intensity at the end of the southern jet is distinctly visible. The extensions of the weaker emission visible to the southwest and northeast from this area correspond very well with the high resolution map at 145 MHz. Despite Faraday rotation, expected to be high at this frequency, the B-vectors are parallel to the jet entering the northern lobe and almost perpendicular to it at the tip of the hook. In this sense the southern lobe is different and the systematic change in the directions of B-vectors is not observed.

The low resolution map which we obtained with the Effelsberg telescope at 2.67 GHz (Fig. 5) shows just the overall shape and the main orientation of 4C 70.19 and was used only to measure the total flux of the source. The extensions to the south and west are due to background radio sources and were not included in the flux measurements (see Sect. 4.2.2). Due to the beam depolarisation and Faraday rotation effects, only the approximate (northeast-southwest) direction of the B-vectors could be obtained.

[5] https://archive.stsci.edu/cgi-bin/dss_form

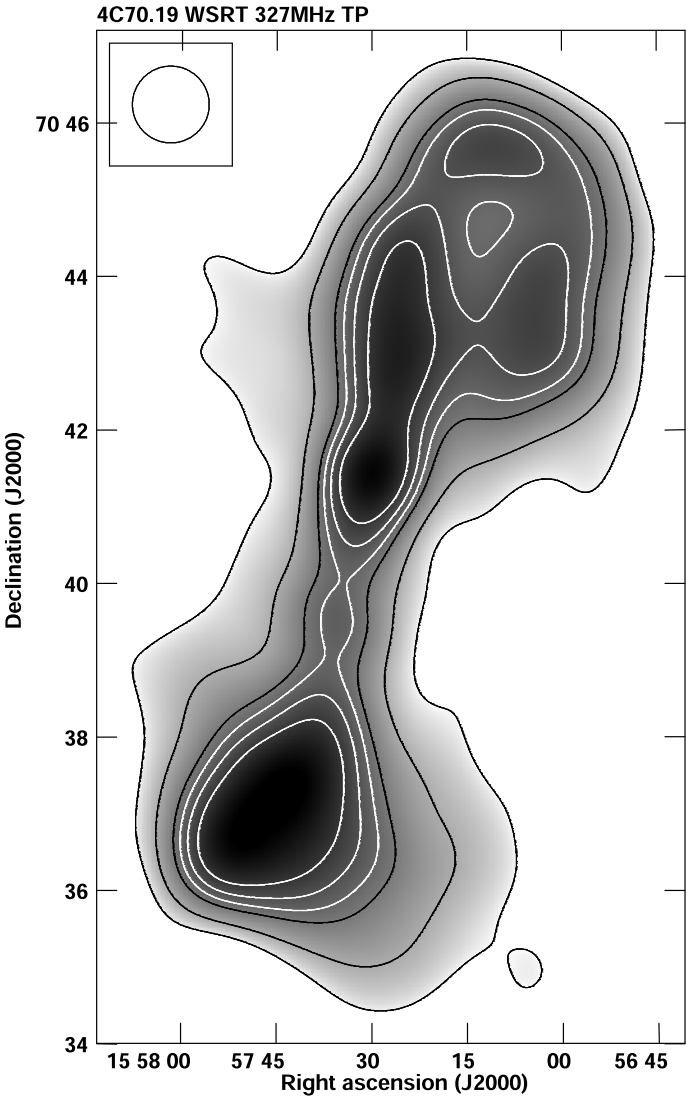

Fig. 3. WENSS map of 4C 70.19 at 327 MHz with contours of (3, 8, 16, 20, 25, and 32) × 7 mJy beam^{-1}. The beam size of 60″ is presented in the upper left corner of the image.

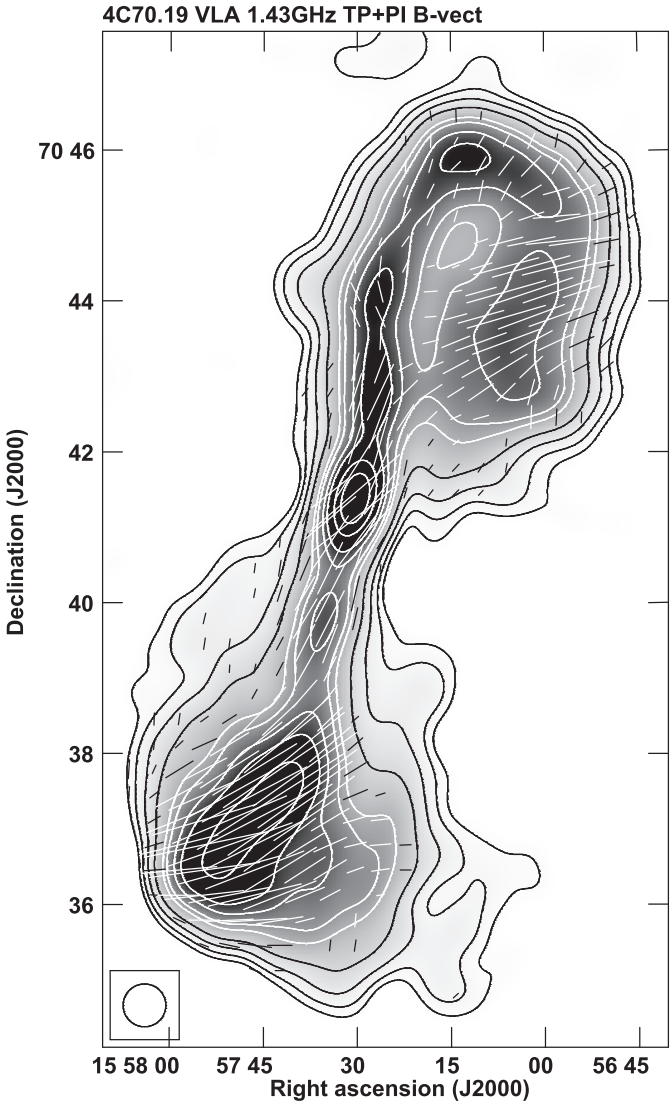

Fig. 4. VLA map of 4C 70.19 at 1.43 GHz. The contours are (3, 6, 12, 24, 48, 64, 96, 128, 192, and 256) × 0.37 mJy beam^{-1}. The lines show the orientation of the magnetic field and a length of 1′ corresponds to polarised emission of 10 mJy beam^{-1}. The beam size of 34″ is presented in the bottom left corner of the image.

The map at 4.85 GHz (Fig. 6) shows primarily the bright jets of 4C 70.19 in similar detail as the 145 MHz LOFAR map. While no large-scale emission is visible, the south-western extension from the end of the southern jet can be seen. At the end of narrow and relatively straight parts of both jets knot-like brightenings (marked with arrows in Fig. 6) are seen, just before the emission becomes more extended. These features are similar to that observed in the radio galaxy NGC 315 (Mack et al. 1997) and will be discussed later (see Sect. 4.2). Very interesting is the orientation of the observed vectors of the magnetic field. Throughout the entire source it is perpendicular to the main axis, except for a part of the northern jet, where it rapidly turns by around 90°and the vectors become parallel to the jet axis and follow the direction of its propagation until the very end, where the vectors are again perpendicular to the jet axis, marking a possible termination of the flow (see Sect. 3.3).

The orientation of the B-vectors at 4.85 GHz is, in fact, very different to what is seen in the map at 1.43 GHz (Fig. 4). Because the relative rotation is close to 90°, we have carefully checked if this could be related to instrumental effects or construction of the maps. Therefore, we analysed both observations (VLA and Effelsberg) separately. We obtained the same results as from the combined data. Taking into account that all polarised intensity and polarisation angle maps were produced in the same manner (also at other frequencies), we conclude that the observed differences between 1.43 and 4.85 GHz maps are of physical origin and should be attributed to Faraday rotation. This will be further discussed in Sect. 4.2.1.

The map at 8.35 GHz (Fig. 7), although having a relatively large beam (∼1.′5), shows the same morphology as the map at 1.43 GHz (Fig. 4). Furthermore, the sensitive single-dish observations allowed us to detect diffuse radio emission around the source, visible not only at the positions of the radio lobes, but also around the central part of the source. Because of the large angular extent of 4C 70.19 this cannot be attributed to beam-smearing of the brighter radio emission. The orientation of the observed B-vectors of the magnetic fields is practically the same

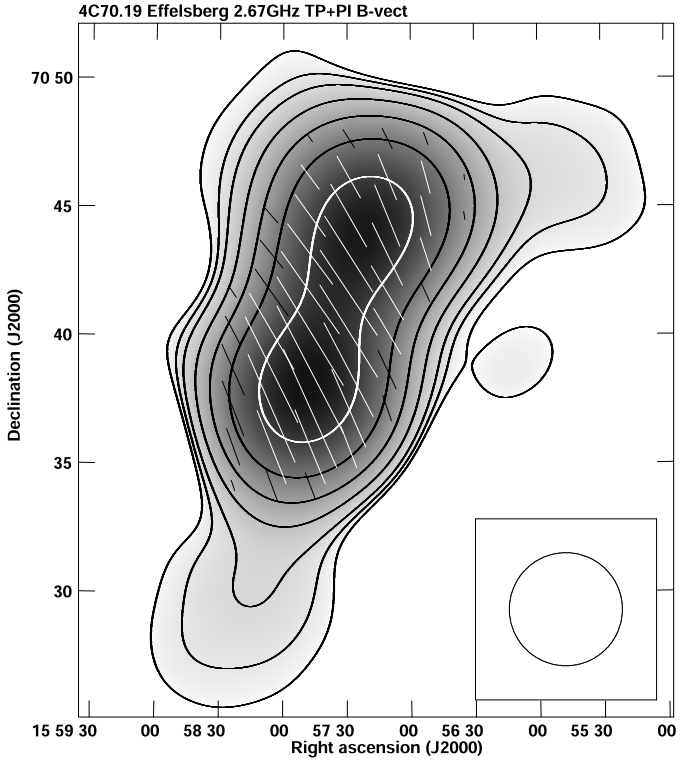

Fig. 5. Effelsberg map of 4C 70.19 at 2.67 GHz. The contours are (3, 5, 8, 16, 32, 64, and 128) × 3.5 mJy beam^{-1}. The lines show the orientation of the magnetic field and a length of 1′ corresponds to polarised emission of 10 mJy beam^{-1}. The beam size of 264″ is presented in the bottom right corner of the image.

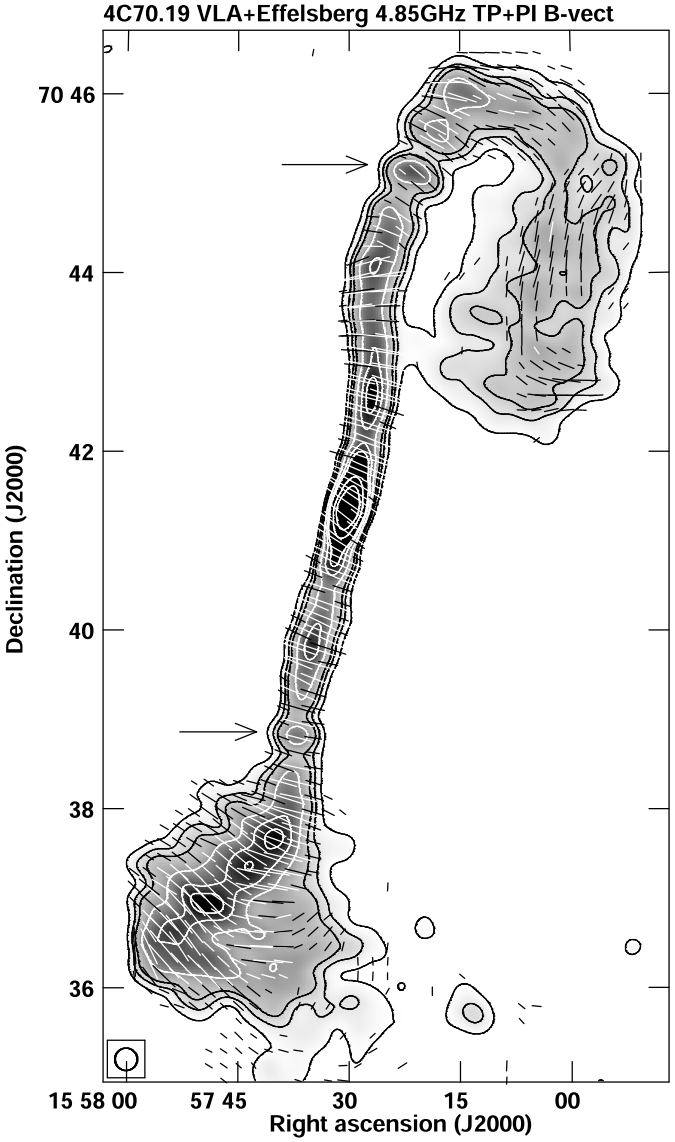

Fig. 6. Merged map of 4C 70.19 at 4.85 GHz produced from the Effelsberg single-dish map and the VLA interferometer maps in C and D configurations. The contours are (3, 6, 9, 16, 25, 32, 64, and 96) × 0.29 mJy beam^{-1}. The lines show the orientation of the magnetic field and a length of 1′ corresponds to polarised emission of 3.3 mJy beam^{-1}. The beam size of 15″ is presented in the bottom left corner of the image. The two arrows point at bright knots of the radio emission (see Sect. 4.2.2 for details).

as that observed at 4.85 GHz and despite the low resolution of the single-dish map, its changes are also clearly visible.

3.2. Large-scale diffuse radio emission

A comparison of all radio maps presented in this paper, as well as those available in the literature, shows that the diffuse emission around 4C 70.19 is only visible in the LOFAR map at 145 MHz (Fig. 1) and in our single-dish Effelsberg map at 8.35 GHz (Fig. 7). Because the latter map shows emission at the highest radio frequency analysed in this paper, these diffuse structures should also be well visible at lower frequencies. Some signs of such emission are also visible in the maps at 327 MHz, and 1.43 GHz, but these maps do not show the large-scale structures. We argue that this is entirely due to sensitivity of the maps. As we mentioned above the large-scale emission outside of the radio jets in the 145 MHz map is likely 'fractured' by a small beam of these observations. Therefore, we convolved this map to the beam of the 8.35 GHz Effelsberg map. As expected, we obtained a map with practically the same extent of the large-scale diffuse emission. This allowed us to estimate the spectral index of this large-scale emission and to calculate the expected surface-brightness at each radio frequency studied in this paper. The estimated sensitivities confirm that only in the single-dish Effelsberg map at 8.35 GHz the large-scale envelope around 4C 70.19 can be detected at the 3σ level. We note here, that the sensitivities typically obtained with the Giant Metrewave Radio Telescope (GMRT) observations at 325 and 610 MHz (e.g. Giacintucci et al. 2011) should allow detection of the large-scale diffuse radio emission around 4C 70.19. To date no such observations exist.

3.3. Propagation of the jets

In Fig. 8 we present the LOFAR map from Fig. 1 but convolved to a resolution of 15″ and processed using the *Sobel* filter that enhances intensity gradients. This allowed to precisely follow the propagation of both jets of 4C 70.19. This propagation is marked with black and red lines for the northern and southern jet, respectively. We note here, that the direction of propagation of the southern jet beyond S4 turning point cannot be clearly traced and the proposed line is likely one of the possible directions. Nevertheless, the proposed direction of the jet

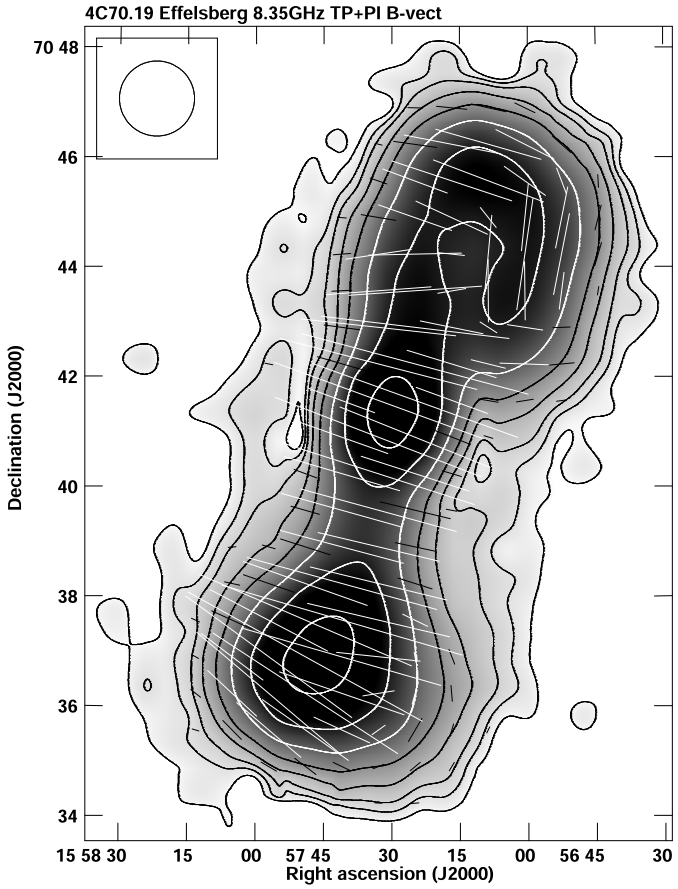

Fig. 7. Map of radio total power at 8.35 GHz from the Effelsberg telescope. The contours are (3, 5, 8, 16, 32, 64, 128, and 256) × 0.31 mJy beam^{-1}. The lines show the orientation of the magnetic field and a length of 1′ correspond to polarised emission of 3.6 mJy beam^{-1}. The beam size of 82″ is presented in the upper left corner of the image.

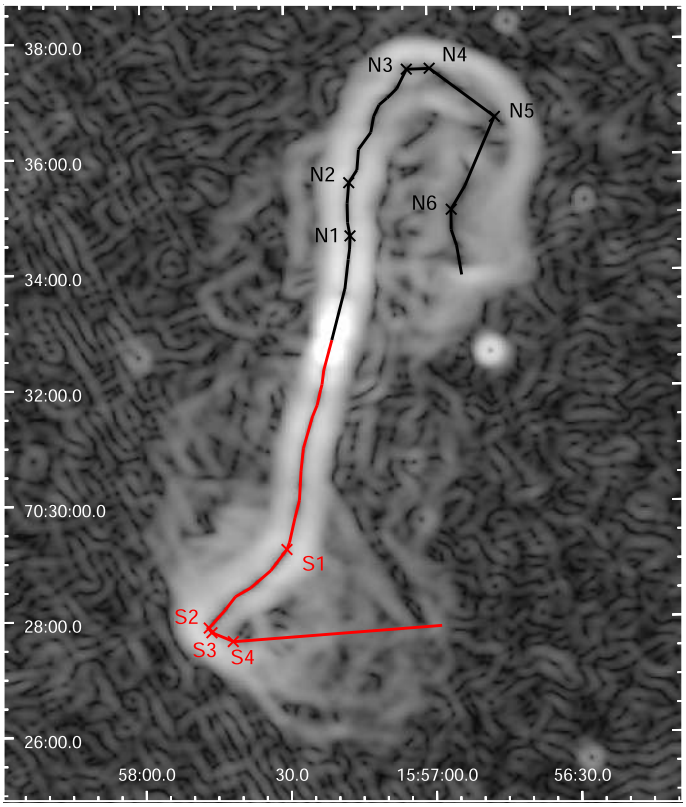

Fig. 8. LOFAR 145 MHz map of 4C 70.19 (Fig. 1) convolved to a beam of 15″ and Sobel filtered with lines showing the propagation of the jets. The main turning points are marked with crosses and are labelled. See Sect. 3.3.

propagation seems to be justified by the orientation of the B-vectors of the magnetic field observed in the high-frequency map of the polarised emission (see the discussion in Sect. 4.2.1).

Frequent changes in the direction of the jet propagation can be noticed and the more significant ones are marked with 'X' and labelled. The profile of the intensity at 145 MHz, measured along the propagation path, is presented in Fig. 9. It shows distinct peaks around 10–15″ from the centre, which correspond to 5–8 kpc, clearly confirming that the central source is not visible at this frequency and that instead two inner and highly symmetric radio features are detected, being likely bases of the jets. Two secondary maxima along both jets are visible around 30–40″ (15–20 kpc) with the northern one slightly closer to the core and about two times brighter than the southern one. The vertical dotted line marks the position of the D_{25} optical luminosity limit of the host galaxy. Although this limit does not have a physical counterpart, around this area a stronger gradient of brightness/ISM density of the host galaxy is expected. This finds its reflection in the profile of the northern jet, whose intensity increases significantly.

The southern jet retains a relatively constant intensity along its path. Around 200″ (100 kpc) from the core, both jets show the same (or comparable) intensities. Beyond this point the intensity of the southern jet increases, until reaching the first turning point (S1), and of the northern jet decreases, roughly by the same amount. Then, the intensity of the southern jet starts to steadily decrease and of the northern jet stays constant, regardless of the significant changes in the direction of its propagation of both jets. It is also worth noting here that with the proposed propagation of the jets, as inferred from the *Sobel*-filtered LOFAR map, both jets of 4C 70.19 are in fact of similar length (each reaching 300 kpc, see lower panel of Fig. 9), and the asymmetric appearance results from projection effects.

4. Discussion

4.1. Galaxy environment

To investigate in more detail the origins of the distortions of 4C 70.19, we used three different catalogues of galaxy groups (Crook et al. 2007; Schombert 2015; Tempel et al. 2016) and compiled a list of all possible members of the group that hosts NGC 6048. There are 12 spectroscopically confirmed candidate galaxies, where NGC 6048 is the brightest group member. Figure 10 shows the NVSS map (at 1.4 GHz) of 4C 70.19 with the group galaxies marked with circles and names. The galaxy closest to NGC 6048, at the distance of around 350 kpc, is IC 1187.

Although even this galaxy seems to be too distant for direct interactions with NGC 6048, there are two more objects, not shown in Fig. 10, that might have influenced its evolution.

The first of them, PGC214442 (RA = $15^{h}57^{m}54\overset{s}{.}0$, Dec = +70°39′47″.14 (J2000.0)), a galaxy of a total B-magnitude of 15.58±0.50 (Klemola et al. 1987), is visible southeast from NGC 6048 (left panel of Fig. 11). It is described by de Vaucouleurs et al. (1976) to form a contact system with

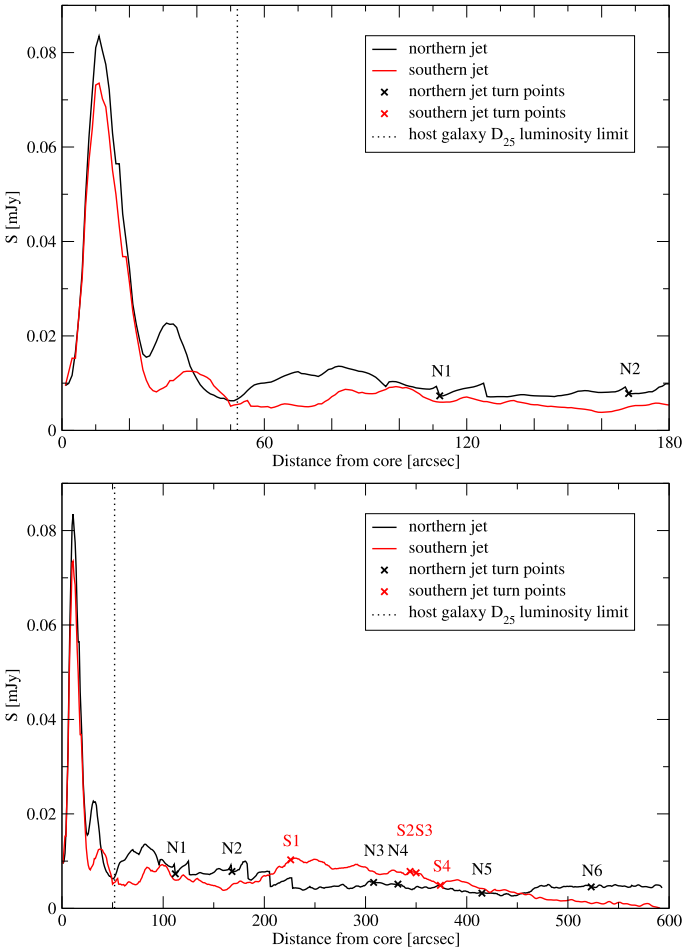

Fig. 9. Intensity profiles of the jets of 4C 70.19. Top: Intensity profiles measured in the LOFAR 145 MHz map (Fig. 1) and the combined VLA+Effelsberg maps at 4850 MHz (Fig. 6) along the propagation lines presented in Fig. 8. The plot is limited to 3′ from the core to better present the inner parts of both jets. Bottom: Intensity profiles as in the upper panel, but along the entire propagation path. In both panels, the vertical dashed line marks the optical D_{25} luminosity limit of the host galaxy NGC 6048 and the main turning points of the jets are marked with crosses and are labelled in the corresponding colour.

NGC 6048. Unfortunately, for this galaxy no spectroscopic redshift has been measured. Its photometric redshift was estimated to $z_{\rm phot} = 0.034 \pm 0.015$ by Dálya et al. (2018). If both galaxies are located at the same distance, their angular separation of 2.′5 would correspond to a linear distance of only 75 kpc. The optical images of PGC214442 from the Pan-STARRS data archive (Flewelling et al. 2020) show the disturbed morphology of this galaxy (left panel of Fig. 11). It has a bright elliptical central part and a disc-like structure with a possible warp inclined to the major axis of the galaxy at around 70 degrees. The disc is elongated towards NGC 6048, which may result from interactions between these two galaxies. Especially, that the halo around NGC 6048, visible in the infrared image from WISE at 3.4 µm (right panel of Fig. 11), is also elongated in the same direction. The infrared image is overlaid with contours of the ROSAT soft X-ray emission. Using the ROSAT HRI countrate within 0.′5 of the core region and assuming a simple power-law model with $\Gamma = 1.6$, we estimated the flux of the central source to be of the order of 3×10^{-13} erg cm^{-2} s^{-1}. At the distance to NGC 6048 this results in a total luminosity of around 4.2×10^{42} erg s^{-1}. Of course, the countrate used includes all the emission from the hot gas in the disc of NGC 6048; however, we do not expect its contribution to be significant. Therefore, at few times 10^{42} erg s^{-1} the central AGN of NGC 6048 is of moderate luminosity, confirming its low level of accretion (see Sect. 1). Both the dust halo around NGC 6048 and the X-ray emission limited to the optical extent of this giant elliptical (right panel of Fig. 11) are likely a result of the recent merger (Sect. 1).

The second candidate source for the interactions is visible southeast from the core of NGC 6048 (Fig. 11). Although no information about this compact object has been found in the literature, its brightness distribution in the image suggests that this is an extra-galactic object rather than a foreground star and so it might be physically present in the close vicinity of NGC 6048. If the same distance to both sources is assumed, they are separated by only 16 kpc. However, for a clear verification of the nature and distance of this compact object, spectroscopic observations are needed. Later in the paper we provide further arguments for the possible interaction of both sources with NGC 6048.

4.2. Radio morphology of the source

The distorted morphology of 4C 70.19 resembles the radio galaxies IC 708 (Vallée et al. 1981) and 3C 31 (Blandford & Icke 1978; Heesen et al. 2018). The winged shape of these two sources was explained as a result of projection effects arising from the orbital motion of the host galaxies interacting with nearby massive objects. As mentioned in Sect. 4.1, NGC 6048 has two relatively close companion galaxies, which may influence its movement through the IGM. On the other hand, the 180° bend of one radio jet and an asymmetric broadening of the other makes this source even more similar to two other radio sources, associated with elliptical galaxies NGC 7626 and NGC 315 (Giacintucci et al. 2011). These distortions of the radio lobes were explained by the authors as interactions with the IGM. Particularly, the FRI source associated with NGC 315 shows slight brightenings at the positions where the radio plumes change their propagation direction (Giacintucci et al. 2011). Similar brightenings are visible (and marked with arrows) in the map of 4C 70.19 at 4.85 GHz (Fig. 6).

To find the inclination of the jet axis of 4C 70.19 that could help to determine the orientation of the radio jets, we analysed the orientation of both pairs of the inner features, using the intensity profiles and the formula used by e.g. Kuźmicz & Jamrozy (2012):

$$i = \left[\mathrm{acos}\left(\frac{1}{\beta_j}\frac{(s-1)}{(s+1)}\right)\right]. \quad (1)$$

This formula assumes that the main cause of asymmetries in a radio source is Doppler boosting. Here, $s = (S_j/S_{cj})^{1/2-\alpha}$ with S_j and S_{cj} are peak flux densities of the structure closer and further from the core, respectively, and β_j is the ratio of the jet velocity to the speed of light. Following Arshakian & Longair (2004) we assumed β_j of 0.54 and the average spectral index α of −0.3. To account for the ambiguous value of the core spectral index we also repeated our calculations with $\alpha = -0.5$. Since the inner structures are almost perfectly symmetric, we compared the calculations for each of them being the closer/further one. Because also the intensity of both features are similar, the resulting inclinations varied by only around 8° with the major axis oriented almost exactly in the sky plane (~86–94°).

For the outer features, however, we obtained an inclination of 58° for $\alpha = -0.5$ and 65° for $\alpha = -0.3$. Within our assumptions made for β_j and α, the 1 mJy accuracy of the amplitudes in the

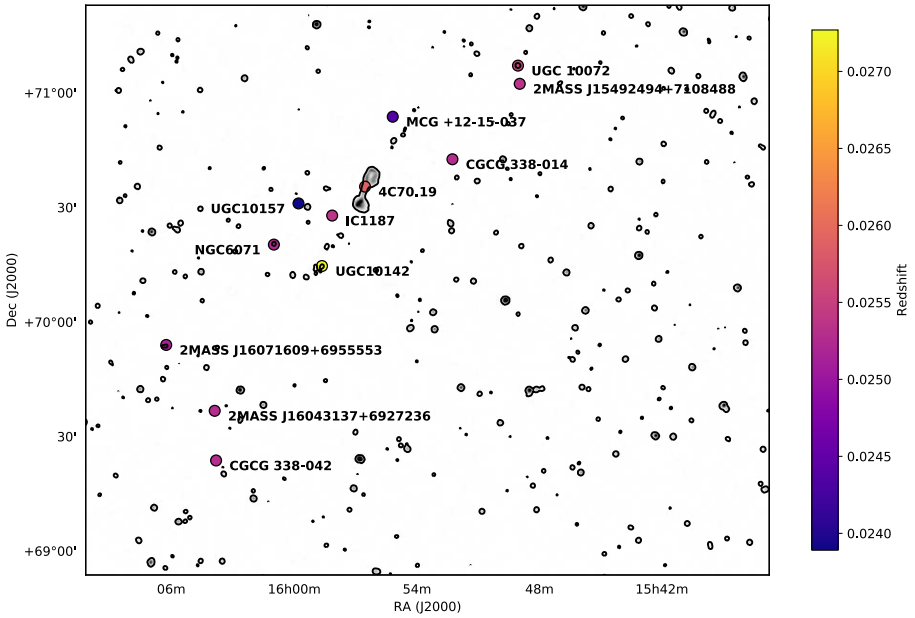

Fig. 10. NVSS map of 4C 70.19 at 1.4 GHz with the group galaxies marked with filled circles and names. The redshifts of individual galaxies are colour coded according to the scale shown on the right. For a clear presentation of the large-scale radio map, only the contour at the level of 2.5 mJy beam^{-1} (5σ) is plotted.

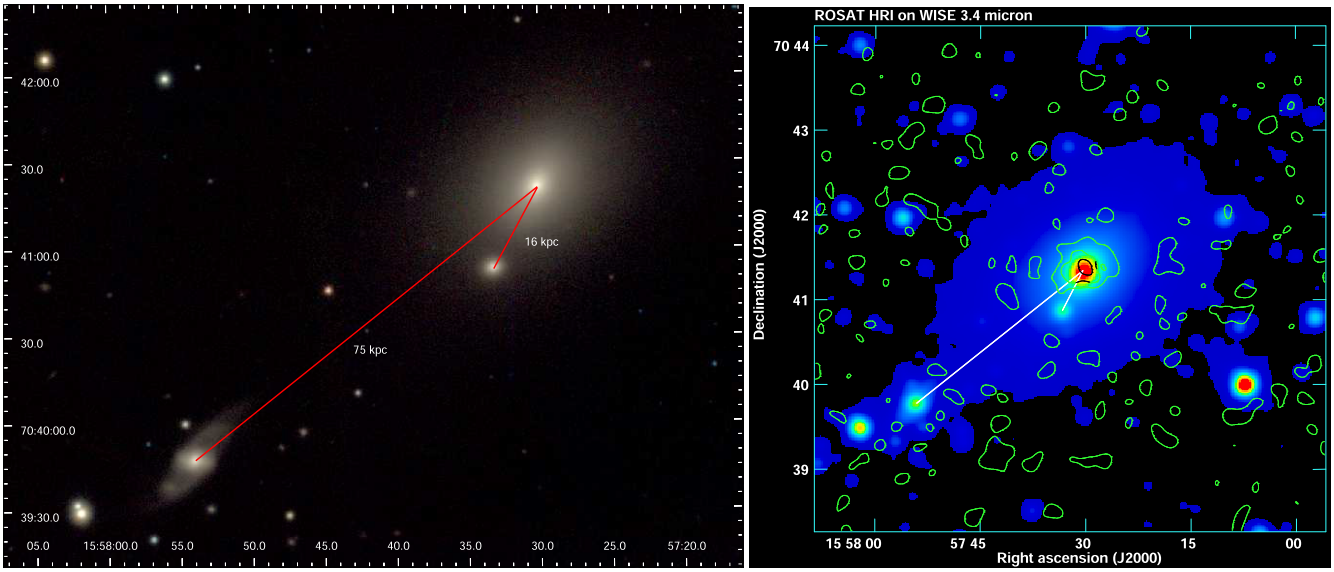

Fig. 11. Optical images of NGC 6048. Left: Pan-STARRS image of the NGC 6048 system in the *r*, *i*, and *z* filters. The red lines mark the projected distances between NGC 6048 (top right) and the halo object, as well as the companion galaxy PGC214442 (bottom left). Right: WISE colour image at 3.4 µm cut at 1σ level overlaid with ROSAT HRI contours at 3, 5, and 8 × the r.m.s.. The white lines correspond to the red ones in the left panel.

profiles results in an uncertainty of the derived angles of 1–2°. This means that the relative difference in orientation between the inner and the outer jet features is of the order of 30°, with the northern jet of 4C 70.19 being oriented towards us. We note here that this change in orientation may be caused by a gas density gradient resulting from leaving the halo of the host galaxy, as well as the existence of the halo object, southeast from the core (see Fig. 11).

As a result, the outward orientation (with regard to the sky-plane) of the southern jet could produce an elongated hot spot-like feature at the position of the jet bend, similar to that visible in the northern side. Then, the enhancement in the observed brightness would be a result of integration of the emission from the bent jet. This is in agreement with the intensity profiles along the jets (Sect. 3.3), which suggests that the south-eastern 'end' of the southern jet is in fact its turning point. This is supported by the increase in intensity of the central part of the southern lobe (lower panel of Fig. 9), which leads to a higher flux integrated in this area and consequently a slightly higher value of the estimated magnetic field strength, when compared to the corresponding part of the northern jet. If we assume that we see the entire northern jet in the sky plane, the beginning of its bend (turning point N3 in Fig. 8) should be roughly at the same distance from the core as the visible end of the southern jet (turning point S2 in Fig. 8). The difference of both extents, as seen in the plot lies below 50″ or 25 kpc. We note here, however, that both jets deviate from the original axis already closer to the core, as visible in Fig. 8. This makes more precise measurements of full

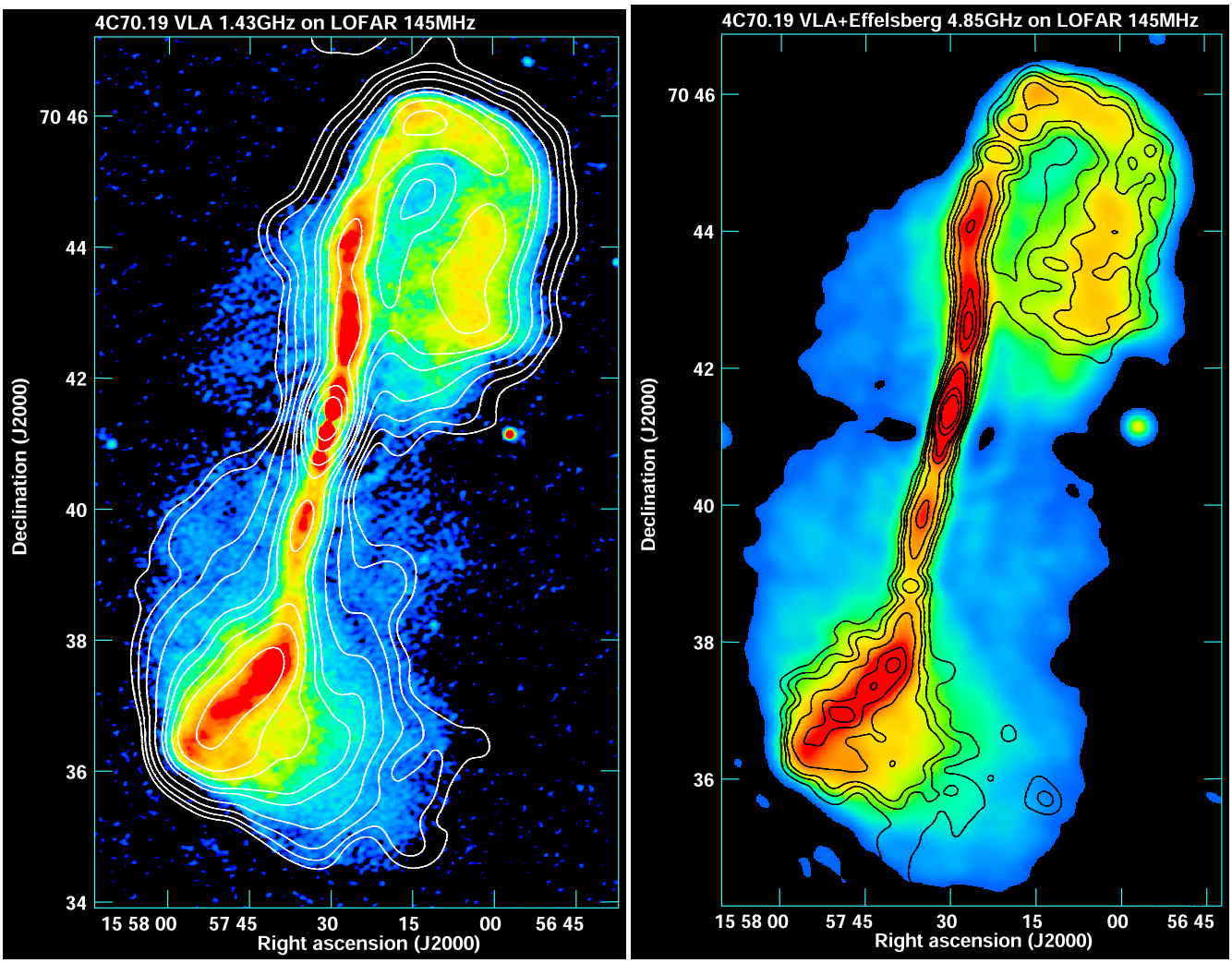

Fig. 12. VLA maps of 4C 70.19 overlaid on its LOFAR map. Left: VLA map of 4C 70.19 at 1.43 GHz from Fig. 4 on the colour image of the LOFAR map at 145 MHz from Fig. 1. The contour levels are (3, 6, 12, 24, 48, 64, 96, 128, 192, and 256) × 0.37 mJy beam^{-1}. Right: VLA+Effelsberg map of 4C 70.19 at 4.85 GHz on the colour image of the LOFAR map at 145 MHz. The latter map was convolved to 15″. The contours are (3, 6, 9, 16, 25, 32, 64, and 96) × 0.29 mJy beam^{-1}.

extent of the jets difficult and the difference below 25 kpc could be attributed to projection effects, as well as differences in the density of the surrounding medium that certainly influence the propagation of the jets.

Both panels of Fig. 12 clearly show that the morphology of 4C 70.19 practically does not change with frequency. The very close correspondence of all radio features is obvious and both jets/lobes have the same extents in both maps at 145 MHz and 4.85 GHz, as well as of the faint large-scale diffuse emission, whose parts are visible in the 1.43 GHz map (left panel of Fig. 12). This correspondence of the radio emission at both ends of the studied spectrum suggests that the observed edges of the emission are rather of physical origin and are not caused by the observational limitations. A straightforward explanation would be the interaction with the surrounding medium, whose pressure does not allow the jets to propagate further and with the combination of the orbital motion within the busy environment of the galaxy group both jets bend. To some extent, this would resemble the famous radio source Virgo A, whose jets interact with the surrounding intra-cluster medium (de Gasperin et al. 2012). This in turn would suggest, that the faint large-scale emission visible in the most sensitive maps (Sect. 3.2) is not a gaseous envelope or halo surrounding 4C 70.19, but the plumes expanding behind the source.

4.2.1. Magnetic fields

As already shown in Sect. 3.1, polarised radio emission obtained from our dedicated Effelsberg observations, as well as the archival VLA data, allowed for a direct analysis of the orientation of magnetic fields in the sky plane. Especially interesting is the behaviour of the magnetic field observed in the maps at high frequencies (Figs. 6 and 7). In the northern jet the orientation of the B-vectors is perpendicular to the jet axis until the bend (points N3-N4 in Fig. 8). In the bend, the degree of polarisation in the outer edge of the jet reaches almost 50% (Fig. 13) and the B-vectors become parallel to the jet axis. Towards the end of the jet, the B-vectors are again perpendicular and the jet terminates with a notable brightening, well visible in the *Sobel*-filtered map (Fig. 8), and an increase in the degree of polarisation (Fig. 13). Such changes of the orientation of the B-vectors are sensitive to gas motions and likely mark the area where the magnetic field is being sheared (the bend) or compressed (jet termination). In such case, the bend of the jet would occur in the region, where the jet

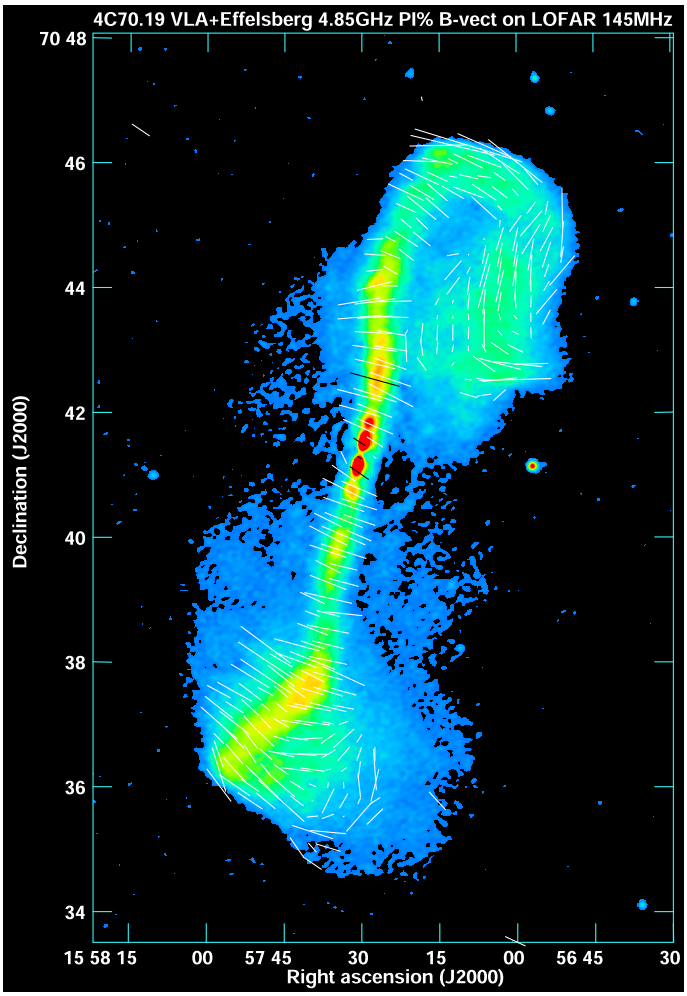

Fig. 13. Map of polarisation degree in 4C 70.19 at 4.85 GHz produced from the Effelsberg single-dish map and the VLA interferometer maps in C and D configurations (Fig. 6) overlaid on the LOFAR 145 MHz map. The lines show the orientation of the magnetic field and a length of 1′ corresponds to degree of polarisation of 50%.

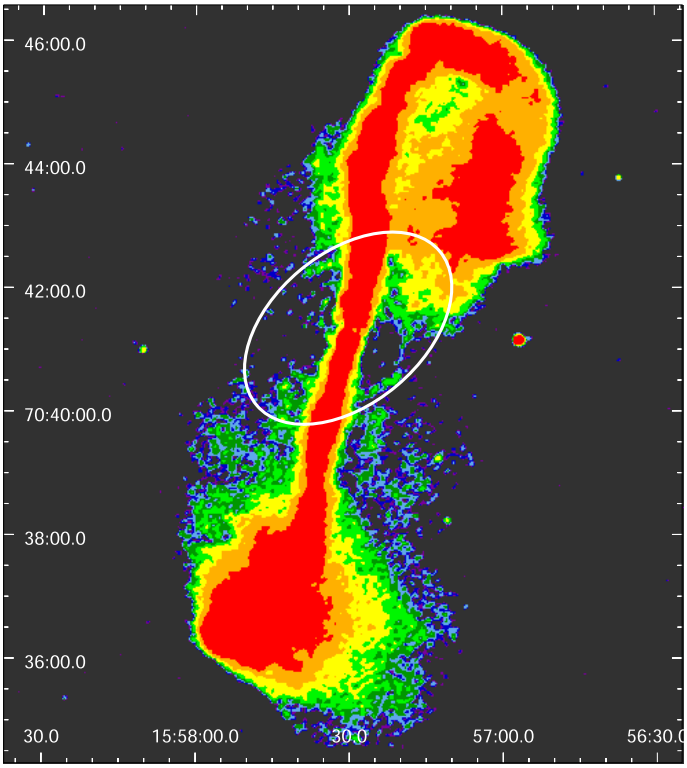

Fig. 14. LOFAR map of 4C 70.19 from Fig. 1. The white ellipse marks the extent of the infrared halo, as visible in the right panel of Fig. 11.

becomes too weak to overcome the pressure of the surrounding medium and is eventually terminated after reaching even denser gas, while moving back towards the host galaxy. The elongated halo around NGC 6048 visible in the infrared map (right panel of Fig. 11) has a shape of an ellipse, whose major axis is pointed almost exactly towards the companion galaxy PGC214442. We overplotted this elliptical halo region on the LOFAR map of 4C 70.19 in Fig. 14. In the north-west the halo reaches the end of the bent northern jet, which could explain the addtional kink and its end, as well as the termination shock, or the deceleration point, beyond which the plume expands freely behind the source in the scenario proposed in the previous section.

In the southern jet, the B-vectors of the magnetic field are perpendicular to its axis along the entire line of propagation, also after the slight bend marked in Fig. 8 as S1. Nevertheless, if we follow the propagation line beyond the last turning point marked (S4), the B-vectors become parallel to the (proposed) jet axis, just like in the northern jet. Also in this case we would expect shearing of the magnetic field at the bend of the jet. This is supported by a slight increase in the degree of polarisation around turning points S2 and S3 (Fig. 13). These findings provide additional arguments for the assumed propagation of the southern jet and that the extension to the south-west is not a diffuse radio lobe but rather the southern jet visible from the side after the bend and extending into a radio plume.

Because we excluded the possibility that the roughly 90° difference in the orientation of the B-vectors seen between 1.43 GHz (Fig. 4) and 4.85 GHz (right panel of Fig. 6) is of instrumental origin (Sect. 3.1), this difference needs a physical explanation. Especially, that the global orientation of the magnetic field visible in the low-resolution map at 2.67 GHz (Fig. 5) seems to be intermediate between those at 1.43 and 4.85 GHz. Both the LOFAR map at 145 MHz (Fig. 1) and the sensitive single-dish Effelsberg map at 8.35 GHz (Fig. 7), as well as our analysis of the surroundings of the host galaxy NGC 6048, presented in the previous section, suggest the presence of magnetised plasma, which could produce Faraday rotation responsible for the observed changes in the orientation of the polarisation angle. The polarised radio data at 4.85 and 8.35 GHz, where the expected Faraday depolarisation is low, allowed us to obtain a map of RM distribution (Fig. 15). The RM values are roughly uniform throughout the source with a mean of $-35\,\mathrm{rad\,m^{-2}}$. The only exception is the area where the northern lobe starts to bend. The rotation measure is around $0\,\mathrm{rad\,m^{-2}}$ at this position. RMs of the order of few tens of $\mathrm{rad\,m^{-2}}$ do not significantly affect the polarisation angle at high frequencies, resulting in uncertainties of only few degrees at 4.85 or 8.35 GHz. To estimate the relative rotation of the polarisation plane between these high frequencies and 1.43 GHz, we use the simple relation between the rotation angle, rotation measure, and wavelength ($\chi = \mathrm{RM} \times \lambda^2$). Then, at 1.43 GHz a rotation measure of $(-)35\,\mathrm{rad\,m^{-2}}$ results in a rotation of the polarisation plane by around 88°, which easily explains the differences of the orientation of the magnetic field vectors mentioned before.

The observed RMs result from the superposition of the intrinsic Faraday rotation around 4C 70.19 and all ‘Faraday

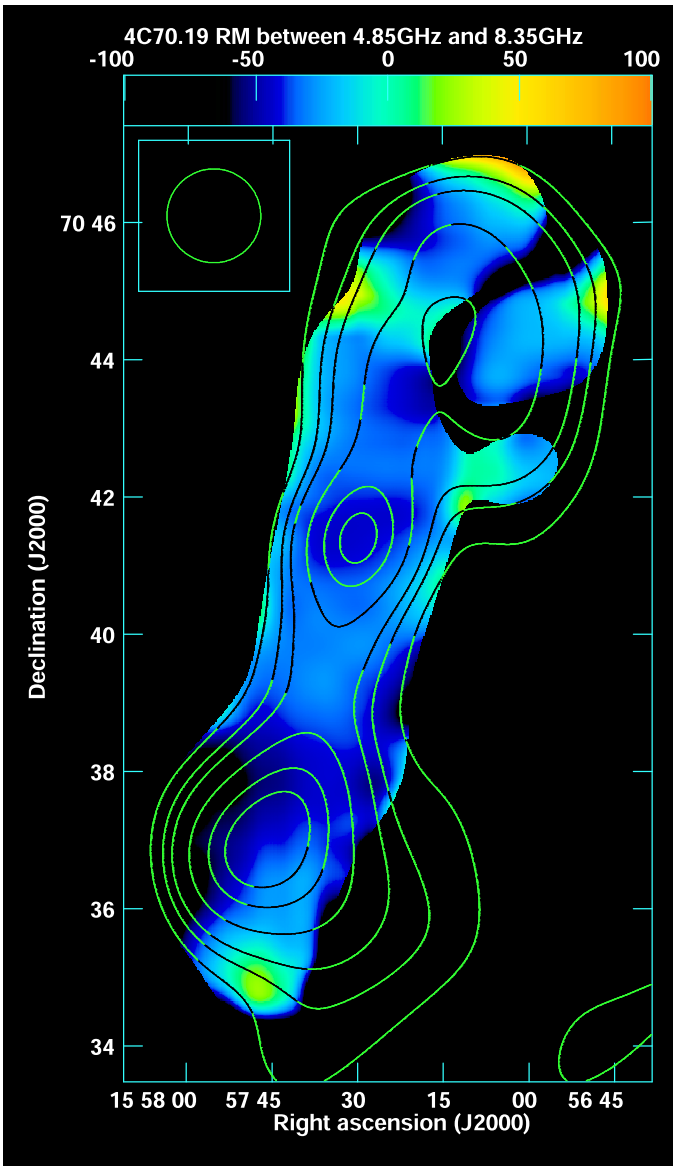

Fig. 15. Rotation measure map of 4C 70.19 between 4.85 and 8.35 GHz. The map is overlaid with contours of the total radio emission map at 4.85 GHz (Fig. 6) convolved to the resolution of the 8.35 GHz map from Fig. 7. The contour levels are (3, 6, 9, 16, 25, 32, 64, and 96) × 3.57 mJy beam^{-1}. The beam size of 82″ is presented in the upper left corner of the image.

screens' along the line-of-sight towards the source. We used the all-sky catalogue of RMs (Taylor et al. 2009) to estimate the contribution only from 4C 70.19. The average RM within 5° from the source is $+7.6 \pm 2.8$ rad m^{-2}, which means that the RM intrinsic to the source are between -45 and -40 rad m^{-2}. Using the strengths of the magnetic field in the radio source, these can be used to estimate local electron densities with the use of the well-known formula for the Faraday-thin source:

$$\mathrm{RM[rad\ m^{-2}]} = 812 \int_0^L n_e[\mathrm{cm^{-3}}] B[\mu\,\mathrm{G}] \cdot dl[\mathrm{kpc}],$$

where RM is rotation measure, n_e is the electron density of the medium, B is the magnetic field component along the line of sight, and dl is the pathlength through the medium.

The strengths of the magnetic field were calculated with the assumption of the minimum energy conditions and following Longair (2011). Our assumptions included the cutoff frequencies of $\upsilon_{\mathrm{min}} = 10$ MHz and $\upsilon_{\mathrm{max}} = 100$ GHz, the filling factor of 1, and the pure electron-positron plasma. The volumes were approximated by a cylindrical shape of 164″ (twice the beam size) in length and a radius of 41″. For the core region we used a spherical shape with a diameter of 82″. Local values of the magnetic field strength in different regions of the source are presented in Fig. 16. The typical magnetic field strengths are 1.5 μG in most regions of the source. The only exception is the core region (2.1 μG) and the central region of the southern lobe (bottom middle graph in Fig. 16, 1.8 μG). We note here, however, that the uncertainty of the derived strengths of the magnetic field is about 0.5 μG.

We used the obtained value of the magnetic field strength to estimate the electron densities of the halo/IGM gas around 4C 70.19 required to produce the RMs observed in our maps. With the above formula, RMs around 40 rad m^{-2} produced within 4C 70.19 (we used the same volumes as for the magnetic field estimates), require electron densities of around 10^{-3} cm^{-3}. Such densities fit well between low-density interstellar medium of galaxies (few 10^{-3} cm^{-3}) and the IGM (a few 10^{-4} cm^{-3}). The derived densities are in fact only lower limits, because our estimates of the magnetic field strengths correspond to the brightest parts of the radio emission, close to the jets. Furthermore, only the line of sight component of the magnetic field is responsible for the observed RMs. Taking both into account, lower values of the magnetic field strengths would require a higher density of the medium to produce the observed RMs. This would make the density of the IGM around 4C 70.19 even closer to the typical values of the low-density ISM, providing another argument for the interactions of NGC 6048 with neighbouring galaxies, as already sugested by the extended and elongated infrared halo (right panel of Fig. 11 and Fig. 14).

4.2.2. Spectral properties

We used all radio data presented in this paper to construct a global radio spectrum of the source (Fig. 17). The mean spectral index α in the 145 MHz–8350 MHz range is -0.61 ± 0.02 ($S \propto \nu^{\alpha}$). We note here that in the two radio maps observed with the single-dish Effelsberg telescope, that is, at 2.67 and 4.85 GHz, the radio morphology of the source was not clearly visible due to a large beam of the observations. This made precise flux measurements difficult because of possible contamination by the background sources. Nevertheless, the map at 4.85 GHz was used only for combination with the high-resolution VLA map (see Sects. 2.1.3 and 3.1), hence no direct flux measurement was performed. For the map at 2.67 GHz with a beam as large as 4′.4, we decided to measure the flux only in the area where the emission in the LOFAR map at 145 MHz convolved to the resolution of the Effelsberg map at 8.35 GHz is above 3σ. The obtained total flux at 2.67 GHz perfectly fits the global spectrum of 4C 70.19 (Fig. 17).

To investigate the distribution of the spectral index throughout the source, we constructed two spectral index maps using the LOFAR 145 MHz, the combined Effelsberg+VLA map at 4.85 GHz, and the Effelsberg 8.35 GHz radio maps. This allowed to obtain a high resolution view of the spectral index in jets and lobes, as well as the large-scale diffuse emission (Fig. 18). Usually, a relatively flat global spectral index (as calculated from the total fluxes measured in our maps) suggests a flat spectrum of the central region and the lobes/hot spots accompanied by a

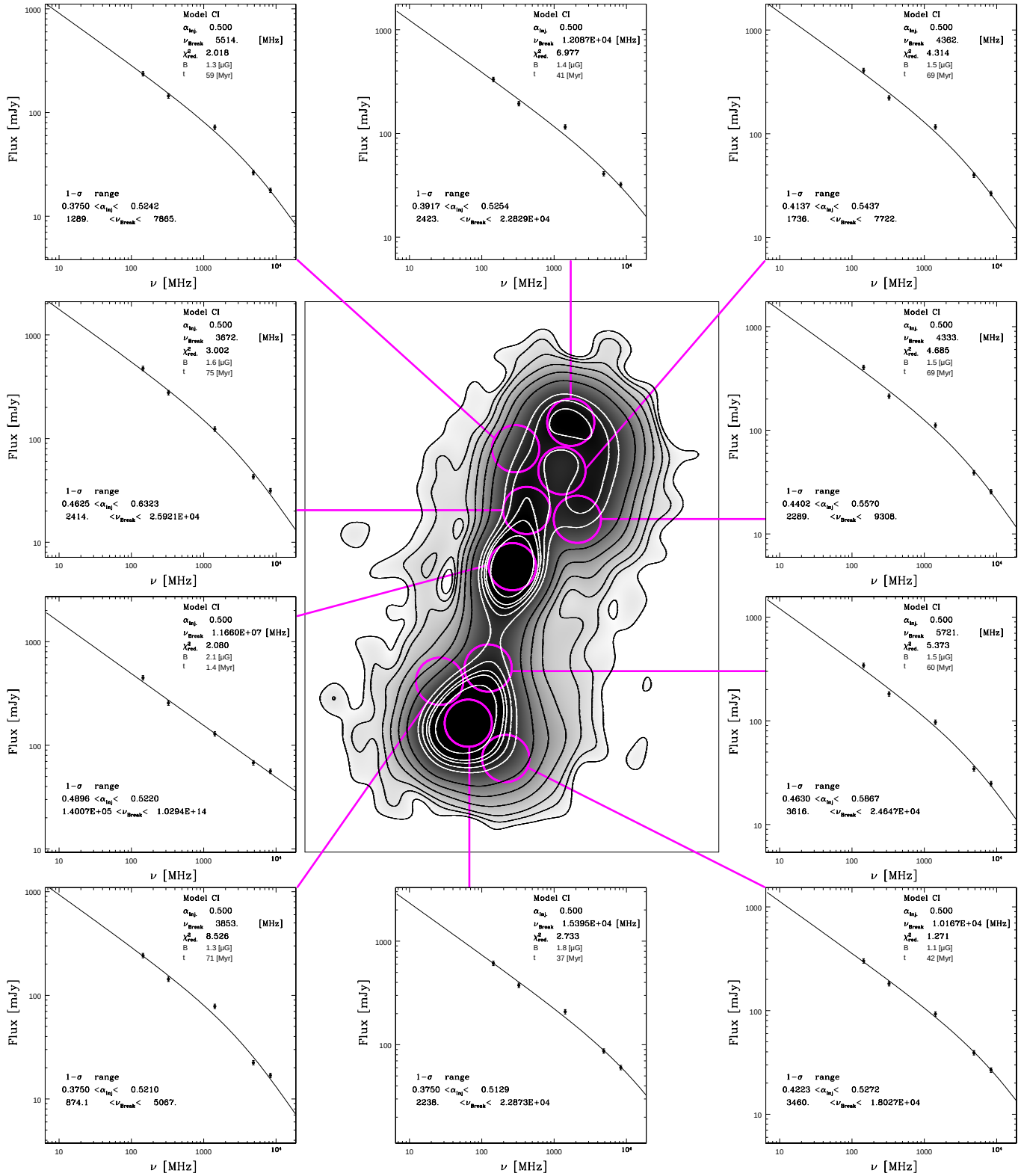

Fig. 16. Effelsberg map of 4C 70.19 from Fig. 7 with the global spectra of selected areas, as marked with the magenta circles (see text for details).

very steep spectrum of the radio cocoon (Miley 1980). In the low resolution spectral index map (left panel of Fig. 18), which includes the large-scale diffuse emission, the areas of the steeper spectral index are found not only close to the core region, suggesting backflow, (e.g. similarly as in the case of 3C 296 and B2 0326+39, Laing et al. 2011), but also in the south-western outskirts of the lobe (e.g. similarly as in the case of the northern extension of NGC 6251, Cantwell et al. 2020). This could mean that the backflow was acting not only towards the centre but also perpendicular to the jet axis, also pointing at the possible bending of the southern jet. Another possibility is that this steepening of the spectral index in the south-west marks the outer parts of the jet, where the emission extends in a plume.

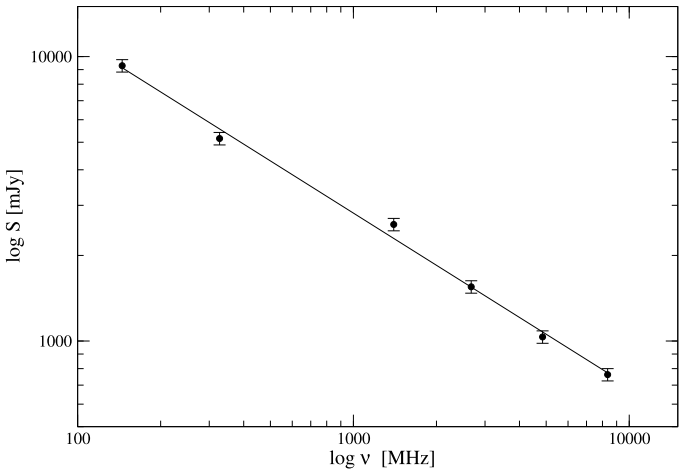

Fig. 17. Integrated spectrum of 4C 70.19.

We also note here that the areas of the very flat or even inverse spectral index at the northern and southeastern boundaries of 4C 70.19 (left panel of Fig. 18) suggest that some of the faint diffuse emission may be lost in the interferometric LOFAR observations. This can be also seen as steep gradients in the emission distribution in the LOFAR map (Fig. 1). Nevertheless, such gradients are visible, within the resolution limits, in all our radio maps, especially in the south-eastern part, which could confirm the bending of the southern jet, so that the visible gradient is just a result of a tangential motion to line of sight.

A more detailed view of the spectral index along the jets of 4C 70.19 is provided by the spectral index map between the LOFAR 145 MHz and the combined 4.85 GHz maps (right panel of Fig. 18) with a resolution of 15″. While the very flat spectral index of the core is not surprising, because it is not visible in the low-frequency map, very interesting are the two compact areas of a flat spectral index found at the end of the (relatively) straight parts of both jets, just before they turn and extend into more diffuse structures. We constructed a profile of the spectral index similar to that of the total intensity (Fig. 19). Although no significant changes of the spectral index with regard to the turning points can be observed, it is worth to note here that both compact areas of a flat spectral index mentioned above are found in almost the same linear distances from their corresponding turning points (N3 and S1 in Fig. 8). These compact regions mark the enhancements of the radio emission visible in the map at 4.85 GHz as bright knots of emission, shown with arrows in Fig. 6. It is possible that in these two regions the jets encounter locally denser medium and decelerate, which causes their subsequent turns and diffusion into plumes.

As we already mentioned in Sect. 4.2, similar bright knots of radio emission, beyond which the jets start to extend into diffuse plumes were also observed in the radio galaxy NGC 315 (Mack et al. 1997). The host of this radio galaxy also resides within a group of galaxies and therefore the presence of IGM with varying density is very probable.

We compared the spectral index of 4C 70.19 with those of the radio galaxies studied by Giacintucci et al. (2011), who investigated interactions of AGNs with the IGM of their host galaxy groups. Six (out of 15) sources from this sample show spectral indices between 235 and 610 MHz of around −0.8 or flatter. Four of them have small linear sizes and are limited to the vicinity of their host galaxies, which suggests relatively young age of these sources. The remaining sources, NGC 7626 and 3C 31, each with a spectral index of −0.81, have larger linear sizes of 185 and 900 kpc, respectively (Giacintucci et al. 2011). 4C 70.19, having a global spectral index of −0.61 and the linear size of 330 kpc, can be therefore considered a similar object. Nevertheless, while 3C 31 has a radio power practically identical to 4C 70.19, NGC 7626 is one order of magnitude weaker. Although both 3C 31 and NGC 7626 show distorted radio tails, their morphology seems to be less complex than that of 4C 70.19 and the bends of their jets are likely observed roughly in the sky-plane. In fact, if we assume the real total extent of 4C 70.19 to be around 600 kpc, as our analyses presented in previous sections suggest, it corresponds to sources like 3C 31 even more closely.

The analyses of the spectral index distribution presented above are performed with the assumption of a constant spectral index in the entire frequency range analysed in this paper. However, the integrated spectral index presented in Fig. 17 suggests that spectral indices can slightly differ between low and high frequency ranges with a distinct change around 1.4 GHz. The total flux of 4C 70.19 at 1.43 GHz is in fact above the global fit, including uncertainties. This flux was obtained with the use of sensitive VLA C-configuration observations that provided sufficient resolution for reliable measurements. Therefore, to study the spectral properties of 4C 70.19 in more detail, we performed the spectral analysis (both global and in selected regions) of 4C 70.19 using all radio maps presented in this paper. We note here, however, that the low-resolution Effelsberg map at 2.67 GHz was used for modelling of the global spectral index only. For the analysis of selected regions, all other maps were convolved to the resolution of the Effelsberg map at 8.35 GHz. Next, the obtained spectra were fitted with the continuous injection (CI; Kardashev 1962) and the Jaffe-Perola (JP; Jaffe & Perola 1973) models using the SYNAGE package (Murgia 1996). For details of the fitting procedure see Jamrozy et al. (2008). The fitting of the theoretical spectra to our data showed that the CI model worked better (lower values of χ^2) than the JP model. For all fits we used a fixed value of $\alpha_{\rm inj} = 0.5$, as the pre-fitting values were always close to 0.5. In fact, this value is predicted by shock theory (Longair 2011) and has been also found for regions of hot spots (e.g. Carilli et al. 1991). The results of our analyses are presented in Fig. 20 (global spectrum) and Fig. 16 (selected regions marked with magenta circles).

In our spectral analysis the regions of the diffuse radio emission were not examined, because this emission was detected only in two of our maps, that is, the LOFAR map at 145 MHz and the Effelsberg map at 8.35 GHz (see Sect. 3.1). The spectral index map between these two frequencies (left panel of Fig. 18) shows that the values there are between −0.8 and −0.9. Our analysis clearly shows, that all spectra, except that for the core region, show a distinct curvature. This means that the synchrotron energy losses of charged particles further from the nucleus are significant and therefore the plasma there is already aged. We expect similar behaviour of the spectral index in areas of the diffuse emission. For most regions the break frequencies are still below the highest frequency that we analyse in this paper, which is the 8.35 GHz Effelsberg data. The derived age of the analysed structures varies from around 40 Myr to 75 Myr in different regions of 4C 70.19, with no visible dependence on the distance from the core. This might be another argument for the complex morphology of this source. For the core region we derived an age of 1.4 Myr only, which points at an ongoing activity of 4C 70.19.

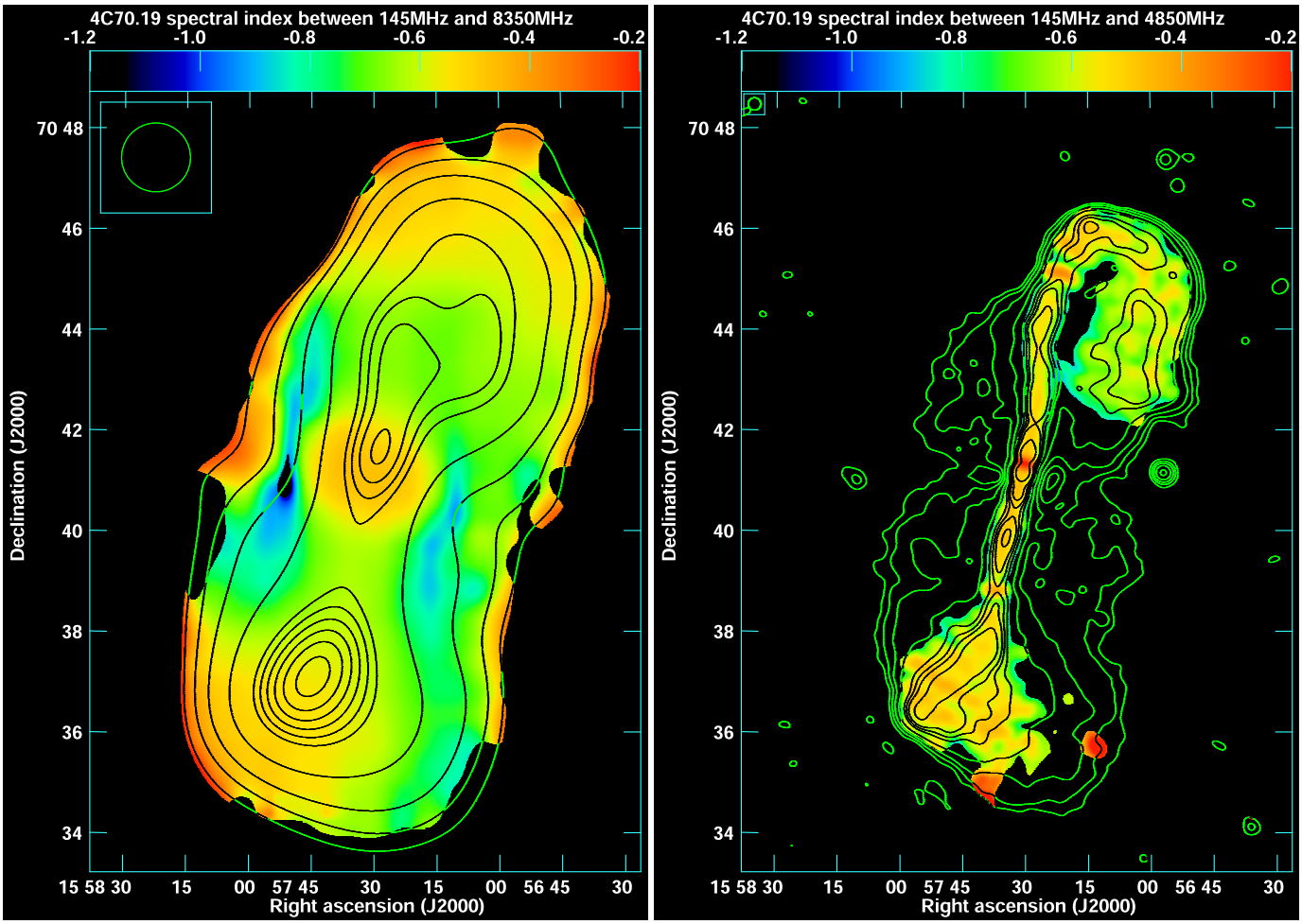

Fig. 18. Spectral index maps of 4C 70.19. Left: Map between 145 MHz (LOFAR) and 8350 MHz (Effelsberg) overlaid with contours of the former map. The contour levels are (3, 10, 30, 100, 250, 300, 350, 400, 450, and 500) × 1.8 mJy beam^{-1}. The beam size of 82″ is presented in the upper left corner of the image. Right: Map between 145 MHz (LOFAR) and 4850 MHz (VLA+Effelsberg) overlaid with contours of the LOFAR map convolved to the resolution of the latter map. The contour levels are (3, 8, 16, 32, 64, 80, 96, 128, and 256) × 0.32 mJy beam^{-1}. The beam size of 15″ is presented in the upper left corner of the image.

5. Summary and conclusions

We investigated the properties of the radio galaxy 4C 70.19, which is associated with the giant elliptical galaxy NGC 6048. Our main conclusions can be summarised as follows:

- The sensitive, high-resolution LOFAR map confirms the morphology of the source visible in the high-frequency maps, showing a bent of the 'hook-like' northern jet and a lack of hot spots.
- In the sensitive LOFAR map at 145 MHz, and in the single-dish Effelsberg map at 8.35 GHz, we detect diffuse radio emission between the central parts of 4C 70.19 and its radio lobes. This low-surface-brightness emission was previously not seen in radio maps, most likely due to their low sensitivity to faint diffuse emission.
- The radio jets seem to rapidly change their orientation when leaving the host galaxy. They are also changing their orientation further out, which may be a result of tidal interactions with the close companions, especially the galaxy PGC214442, which is present within the elongated infrared halo of NGC 6048.
- The propagation of both jets can be explained as a combination of the tidal interactions of the host galaxy with its companions and the orbital motion within the IGM.
- We propose that the elongated brightening along the end of the southern jet is likely a bend, and is similar to that of the northern jet, but occurs outwards.
- The decreasing power of the jets leads to the interaction with the surrounding medium and a consequent change in the direction of propagation, manifesting as the shearing of the magnetic field. This shearing changes the orientation of the magnetic field with respect to the jet axis from perpendicular to parallel at the bends.
- Faraday rotation measurements suggest that the density of the medium around 4C 70.19 is of the order of 10^{-3} cm^{-3}, which is in close agreement with the transition between the outer parts of the halo of the host galaxy NGC 6048 and the IGM.
- We analysed the spectral index of this source for the first time. The global spectral index of 4C 70.19 ($\alpha = -0.61$) is relatively flat. For different parts of the source, the local spectral index changes by no more than about 0.2. This suggests that acceleration and re-acceleration processes should dominate throughout the source, as suggested by the spectral index of the faint diffuse emission around the source.
- The break frequencies calculated for regions in different parts of 4C 70.19 are at a few GHz. The magnetic fields are roughly uniform throughout the source, reaching a value of about

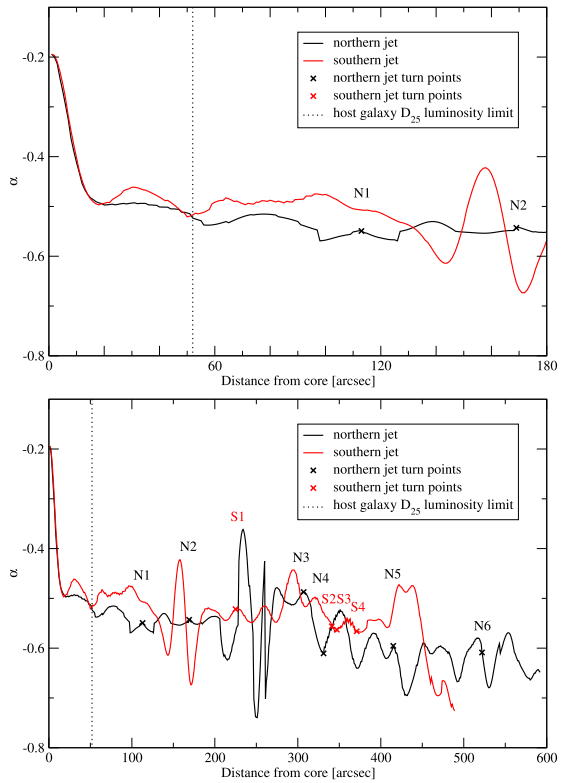

Fig. 19. Spectral index profiles along the jet propagation lines of 4C 70.19. Top: Profiles measured in the spectral index map between 145 and 4850 MHz (left panel of Fig. 18). The plot is limited to 3′ from the core to better present the inner parts of the jets. Bottom: Profiles as in the upper panel, but along the entire propagation path. In both panels the vertical dashed line marks the optical D_{25} luminosity limit of the host galaxy NGC 6048 and the main turning points of the jets are marked with crosses and labelled in corresponding colour.

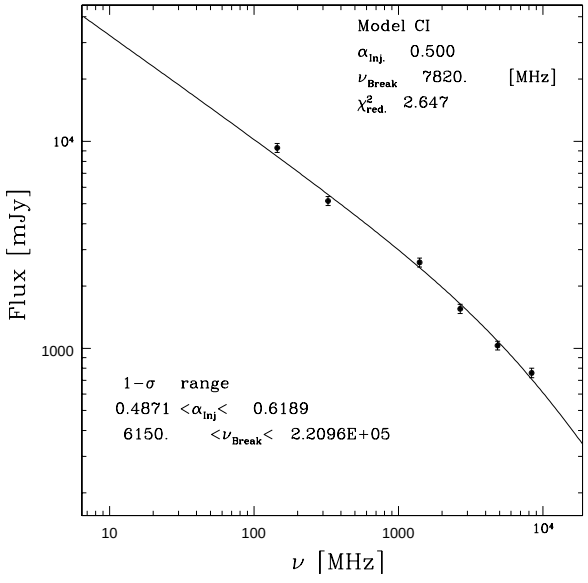

Fig. 20. Modelled global spectrum of 4C 70.19.

1.5 μG, except for the core region and the bright region within the postulated bend of the southern jet.
– Our analyses suggest that 4C 70.19 does not show any physical asymmetries, and its de-projected size could be as large as 600 kpc. We conclude that the diffuse emission around the jets and lobes of 4C 70.19 are radio plumes expanding outwards, behind the source.

The observations and analyses presented in this paper provide a consistent explanation of the intriguing radio morphology of 4C 70.19; however, additional data would certainly allow further verification of our findings. These data include sensitive high-resolution observations at both low (GMRT) and high (VLA) frequencies, deep X-ray imaging of NGC 6048 and its surroundings, as well as spectroscopic observations of the group galaxies in the vicinity of 4C 70.19.

Acknowledgements. The authors are grateful to Alex Krauss for the possibility to perform additional observations with the Effelsberg telescope and Wojciech Jurusik for substantial help with the LOFAR data reduction. We thank Raffaella Morganti for helpful discussions, as well as the anonymous referee for the comments, that helped to improve this paper. M.J. is grateful to Matteo Murgia for access to the SYNAGE software. M.J. acknowledges the Polish National Science Centre grant No: 2018/29/B/ST9/01793. MJH acknowledges support from the UK STFC [ST/V000624/1]. This paper is based (in part) on data obtained with the International LOFAR Telescope (ILT). LOFAR (van Haarlem et al. 2013) is the Low Frequency Array designed and constructed by ASTRON. It has observing, data processing, and data storage facilities in several countries, that are owned by various parties (each with their own funding sources), and that are collectively operated by the ILT foundation under a joint scientific policy. The ILT resources have benefited from the following recent major funding sources: CNRS-INSU, Observatoire de Paris and Université d'Orléans, France; BMBF, MIWF-NRW, MPG, Germany; Science Foundation Ireland (SFI), Department of Business, Enterprise and Innovation (DBEI), Ireland; NWO, The Netherlands; The Science and Technology Facilities Council, UK; Ministry of Science and Higher Education, Poland. The Pan-STARRS1 Surveys (PS1) and the PS1 public science archive have been made possible through contributions by the Institute for Astronomy, the University of Hawaii, the Pan-STARRS Project Office, the Max-Planck Society and its participating institutes, the Max Planck Institute for Astronomy, Heidelberg and the Max Planck Institute for Extraterrestrial Physics, Garching, The Johns Hopkins University, Durham University, the University of Edinburgh, the Queen's University Belfast, the Harvard-Smithsonian Center for Astrophysics, the Las Cumbres Observatory Global Telescope Network Incorporated, the National Central University of Taiwan, the Space Telescope Science Institute, the National Aeronautics and Space Administration under Grant No. NNX08AR22G issued through the Planetary Science Division of the NASA Science Mission Directorate, the National Science Foundation Grant No. AST-1238877, the University of Maryland, Eotvos Lorand University (ELTE), the Los Alamos National Laboratory, and the Gordon and Betty Moore Foundation.

References

Arshakian, T. G., & Longair, M. S. 2004, MNRAS, 351, 727
Baars, J. W. M., Genzel, R., Pauliny-Toth, I. I. K., & Witzel, A. 1977, A&A, 61, 99
Blandford, R. D., & Icke, V. 1978, MNRAS, 185, 527
Cantwell, T. M., Bray, J. D., Croston, J. H., et al. 2020, MNRAS, 495, 143
Carilli, C. L., Perley, R. A., Dreher, J. W., & Leahy, J. P. 1991, ApJ, 383, 554
Clark, B. G. 1980, A&A, 89, 377
Crook, A. C., Huchra, J. P., Martimbeau, N., et al. 2007, ApJ, 655, 790
Dabhade, P., Mahato, M., Bagchi, J., et al. 2020, A&A, 642, A153
Dálya, G., Galgóczi, G., Dobos, L., et al. 2018, MNRAS, 479, 2374
de Gasperin, F., Orrú, E., Murgia, M., et al. 2012, A&A, 547, A56
de Gasperin, F., Dijkema, T. J., Drabent, A., et al. 2019, A&A, 622, A5
de Vaucouleurs, G., de Vaucouleurs, A., & Corwin, J. R. 1976, Second reference catalogue of bright galaxies, 1976
Fanaroff, B. L., & Riley, J. M. 1974, MNRAS, 167, 31P
Flewelling, H. A., Magnier, E. A., Chambers, K. C., et al. 2020, ApJS, 251, 7
Gabriel, C., Denby, M., Fyfe, D. J., et al. 2004, ASP Conf. Ser., 314, 759
Giacintucci, S., O'Sullivan, E., Vrtilek, J., et al. 2011, ApJ, 732, 95
Gioia, I. M., Gregorini, L., & Klein, U. 1982, A&A, 116, 164
Heald, G. H., Pizzo, R. F., Orrú, E., et al. 2015, A&A, 582, A123
Heesen, V., Croston, J. H., Morganti, R., et al. 2018, MNRAS, 474, 5049
Hine, R. G., & Longair, M. S. 1979, MNRAS, 188, 111
Horellou, C., Intema, H. T., Smolčić, V., et al. 2018, A&A, 620, A19
Jaffe, W. J., & Perola, G. C. 1973, A&A, 26, 423
Jamrozy, M., Konar, C., Machalski, J., & Saikia, D. J. 2008, MNRAS, 385, 1286
Kardashev, N. S. 1962, Sov. Ast., 6, 317
Klemola, A. R., Jones, B. F., & Hanson, R. B. 1987, AJ, 94, 501
Kuźmicz, A., & Jamrozy, M. 2012, MNRAS, 426, 851

Kuźmicz, A., Jamrozy, M., Kozieł-Wierzbowska, D., & Weżgowiec, M. 2017, MNRAS, 471, 3806
Kuźmicz, A., Jamrozy, M., Bronarska, K., Janda-Boczar, K., & Saikia, D. J. 2018, ApJS, 238, 9
Laing, R. A., Guidetti, D., Bridle, A. H., Parma, P., & Bondi, M. 2011, MNRAS, 417, 2789
Lara, L., Cotton, W. D., Feretti, L., et al. 2001, A&A, 370, 409
Longair, M. S. 2011, High Energy Astrophysics (Cambridge, UK: Cambridge University Press)
Machalski, J., Kozieł-Wierzbowska, D., Jamrozy, M., & Saikia, D. J. 2008, ApJ, 679, 149
Mack, K. H., Klein, U., O'Dea, C. P., & Willis, A. G. 1997, A&AS, 123, 423
Mahatma, V. H., Hardcastle, M. J., Williams, W. L., et al. 2019, A&A, 622, A13
Miley, G. 1980, ARA&A, 18, 165
Murgia, M. 1996, Ph.D. Thesis, Laurea Thesis, Univ. of Bologna
Nandi, S., & Saikia, D. J. 2012, Bull. Astron. Soc. India, 40, 121
Pfeffermann, E., Briel, U. G., Hippmann, H., et al. 1987, Proc. SPIE, 733, 519
Saikia, D. J., & Jamrozy, M. 2009, Bull. Astron. Soc. India, 37, 63
Schombert, J. M. 2015, AJ, 150, 162
Shimwell, T. W., Röttgering, H. J. A., Best, P. N., et al. 2017, A&A, 598, A104
Shimwell, T. W., Tasse, C., Hardcastle, M. J., et al. 2019, A&A, 622, A1
Smirnov, O. M., & Tasse, C. 2015, MNRAS, 449, 2668
Spergel, D. N., Verde, L., Peiris, H. V., et al. 2003, ApJS, 148, 175
Stickel, M., Kuehr, H., & Fried, J. W. 1993, A&AS, 97, 483
Tasse, C. 2014, A&A, 566, A127
Tasse, C., Hugo, B., Mirmont, M., et al. 2018, A&A, 611, A87
Tasse, C., Shimwell, T., Hardcastle, M. J., et al. 2021, A&A, 648, A1
Taylor, A. R., Stil, J. M., & Sunstrum, C. 2009, ApJ, 702, 1230
Tempel, E., Kipper, R., Tamm, A., et al. 2016, A&A, 588, A14
Truemper, J. 1982, Adv. Space Res., 2, 241
Vallée, J. P., Bridle, A. H., & Wilson, A. S. 1981, ApJ, 250, 66
van Haarlem, M. P., Wise, M. W., Gunst, A. W., et al. 2013, A&A, 556, A2
van Weeren, R. J., Williams, W. L., Hardcastle, M. J., et al. 2016, ApJS, 223, 2
Weżgowiec, M., Urbanik, M., Vollmer, B., et al. 2007, A&A, 471, 93
Williams, W. L., van Weeren, R. J., Röttgering, H. J. A., et al. 2016, MNRAS, 460, 2385
Wright, E. L., Eisenhardt, P. R. M., Mainzer, A. K., et al. 2010, AJ, 140, 1868